# Isomers and high-spin structures in the $N = 81$ isotones $^{135}$Xe and $^{137}$Ba

A. Vogt,[1,*] B. Birkenbach,[1] P. Reiter,[1] A. Blazhev,[1] M. Siciliano,[2,3] K. Hadyńska-Klęk,[3] J. J. Valiente-Dobón,[3] C. Wheldon,[4] E. Teruya,[5] N. Yoshinaga,[5] K. Arnswald,[1] D. Bazzacco,[6] M. Bowry,[7] A. Bracco,[8] B. Bruyneel,[9] R. S. Chakrawarthy,[10] R. Chapman,[11] D. Cline,[12] L. Corradi,[3] F. C. L Crespi,[8] M. Cromaz,[13] G. de Angelis,[3] J. Eberth,[1] P. Fallon,[13] E. Farnea,[6,†] E. Fioretto,[3] S. J. Freeman,[10] B. Fu,[1] A. Gadea,[14] K. Geibel,[1] W. Gelletly,[7] A. Gengelbach,[15] A. Giaz,[8] A. Görgen,[16,17,13] A. Gottardo,[3] A. B. Hayes,[12] H. Hess,[1] R. Hirsch,[1] H. Hua,[12] P. R. John,[2,6] J. Jolie,[1] A. Jungclaus,[18] L. Kaya,[1] W. Korten,[17] I. Y. Lee,[13] S. Leoni,[8] L. Lewandowski,[1] X. Liang,[11] S. Lunardi,[2,6] A. O. Macchiavelli,[13] R. Menegazzo,[6] D. Mengoni,[19,2,6] C. Michelagnoli,[2,6,‡] T. Mijatović,[20] G. Montagnoli,[2,6] D. Montanari,[2,6,§] C. Müller-Gatermann,[1] D. Napoli,[3] C. J. Pearson,[7,‖] L. Pellegri,[8] Zs. Podolyák,[7] G. Pollarolo,[21] A. Pullia,[8] M. Queiser,[1] F. Radeck,[1] F. Recchia,[2,6] P. H. Regan,[7,22] D. Rosiak,[1] N. Saed-Samii,[1] E. Şahin,[3,¶] F. Scarlassara,[2,6] D. Schneiders,[1] M. Seidlitz,[1] B. Siebeck,[1] G. Sletten,[23] J. F. Smith,[11] P.-A. Söderström,[15,#] A. M. Stefanini,[3] T. Steinbach,[1] O. Stezowski,[24] S. Szilner,[20] B. Szpak,[25] R. Teng,[12] C. Ur,[6] V. Vandone,[8] D. D. Warner,[26,†] A. Wiens,[1] C. Y. Wu,[12,**] and K. O. Zell[1]

[1]*Institut für Kernphysik, Universität zu Köln, D-50937 Köln, Germany*
[2]*Dipartimento di Fisica e Astronomia, Università di Padova, I-35131 Padova, Italy*
[3]*Istituto Nazionale di Fisica Nucleare, Laboratori Nazionali di Legnaro, I-35020 Legnaro, Italy*
[4]*School of Physics and Astronomy, University of Birmingham, Birmingham B15 2TT, United Kingdom*
[5]*Department of Physics, Saitama University, Saitama City 338-8570, Japan*
[6]*Istituto Nazionale di Fisica Nucleare, Sezione di Padova, I-35131 Padova, Italy*
[7]*Department of Physics, University of Surrey, Guildford, Surrey GU2 7XH, United Kingdom*
[8]*Dipartimento di Fisica, Università di Milano and INFN Sezione di Milano, I-20133 Milano, Italy*
[9]*CEA Saclay, Service de Physique Nucleaire, F-91191 Gif-sur-Yvette, France*
[10]*Department of Physics and Astronomy, Schuster Laboratory, University of Manchester, Manchester M13 9PL, United Kingdom*
[11]*SUPA, School of Engineering and Computing, University of the West of Scotland, Paisley PA1 2BE, United Kingdom*
[12]*Department of Physics, University of Rochester, Rochester, New York 14627, USA*
[13]*Lawrence Berkeley National Laboratory, Berkeley, California 94720, USA*
[14]*Instituto de Física Corpuscular, CSIC-Universidad de Valencia, E-46071 Valencia, Spain*
[15]*Department of Physics and Astronomy, Uppsala University, SE-75121 Uppsala, Sweden*
[16]*Department of Physics, University of Oslo, P.O. Box 1048 Blindern, N-0316 Oslo, Norway*
[17]*Institut de Recherche sur les lois Fondamentales de l'Univers - IRFU, CEA, Université Paris-Saclay, F-91191 Gif-sur-Yvette Cedex, France*
[18]*Instituto de Estructura de la Materia, CSIC, Madrid, E-28006 Madrid, Spain*
[19]*Nuclear Physics Research Group, University of the West of Scotland, High Street, Paisley PA1 2BE, Scotland, United Kingdom*
[20]*Ruđer Bošković Institute, HR-10 002 Zagreb, Croatia*
[21]*Dipartimento di Fisica Teorica dell'Università di Torino and INFN, I-10125 Torino, Italy*
[22]*Radioactivity Group, National Physical Laboratory, Teddington, Middlesex, TW11 0LW, United Kingdom*
[23]*The Niels Bohr Institute, University of Copenhagen, Blegdamsvej 17, 2100 Copenhagen, Denmark*
[24]*Université de Lyon, Université Lyon-1, CNRS/IN2P3, UMR5822, IPNL, F-69622 Villeurbanne Cedex, France*
[25]*Henryk Niewodniczański Institute of Nuclear Physics PAN, PL-31342 Kraków, Poland*
[26]*CCLRC Daresbury Laboratory, Warrington WA4 4AD, United Kingdom*

(Received 22 December 2016; published 15 February 2017)

The high-spin structures and isomers of the $N = 81$ isotones $^{135}$Xe and $^{137}$Ba are investigated after multinucleon-transfer (MNT) and fusion-evaporation reactions. Both nuclei are populated (i) in $^{136}$Xe + $^{238}$U and (ii) $^{136}$Xe + $^{208}$Pb MNT reactions employing the high-resolution Advanced Gamma Tracking Array (AGATA) coupled to the magnetic spectrometer PRISMA, (iii) in the $^{136}$Xe + $^{198}$Pt MNT reaction employing the $\gamma$-ray array GAMMASPHERE in combination with the gas-detector array CHICO, and (iv) via a $^{11}$B + $^{130}$Te fusion-evaporation reaction with the HORUS $\gamma$-ray array at the University of Cologne. The high-spin level schemes

*Corresponding author: andreas.vogt@ikp.uni-koeln.de
†Deceased.
‡Institut Laue-Langevin (ILL), 38042 Grenoble Cedex 9, France.
§USIAS – Universite de Strasbourg, IPHC-CNRS, F-67037 Strasbourg Cedex 2, France.
‖TRIUMF, 4004 Wesbrook Mall, Vancouver, British Columbia, V6T 2A3 Canada.
¶Department of Physics, University of Oslo, P.O. Box 1048 Blindern, N-0316 Oslo, Norway.
#RIKEN Nishina Center, Wako, 351-0198 Saitama, Japan.
**Lawrence Livermore National Laboratory, Livermore, California 94551, USA.

 

of $^{135}$Xe and $^{137}$Ba are considerably extended to higher energies. The 2058-keV $(19/2^-)$ state in $^{135}$Xe is identified as an isomer, closing a gap in the systematics along the $N = 81$ isotones. Its half-life is measured to be 9.0(9) ns, corresponding to a reduced transition probability of $B(E2, 19/2^- \rightarrow 15/2^-) = 0.52(6)$ W.u. The experimentally deduced reduced transition probabilities of the isomeric states are compared to shell-model predictions. Latest shell-model calculations reproduce the experimental findings generally well and provide guidance to the interpretation of the new levels.

DOI: 10.1103/PhysRevC.95.024316

## I. INTRODUCTION

The nuclear structure of high-spin states in the vicinity of the $N = 82$ magic number is a benchmark for nuclear shell-model (SM) calculations based on modern effective interactions in the region above the doubly magic nucleus $^{132}$Sn. $N = 81$ nuclei with one neutron hole with respect to the closed neutron shell offer an especially fertile study ground for the ingredients of nucleon-nucleon effective interactions and nucleon-nucleon correlations in the shell-model framework. The $N = 81$ chain is accessible by advanced large-scale shell-model calculations. Several effective interactions have been developed recently [1–5], heading toward a unified description of the $50 \leqslant N, Z \leqslant 82$ region. Particularly, neutron-neutron and proton-proton correlations up to highest spins were thoroughly investigated along the semimagic $Z = 50$ isotopes [6,7] as well as the semimagic $N = 82$ [8,9] isotones. However, the evolution of the proton-neutron force remains an ongoing subject of discussion in this region. Tests of all components of effective interactions, including the proton-neutron correlations as a function of isospin and spin, have to be performed, either in nuclei having several neutron holes in the presence of a few proton particles, or vice versa with few neutron holes and a larger number of protons. Comprehensive studies were carried out, for example, along the Te isotopes [10–12].

This work focuses on the $N = 81$ isotones $^{135}$Xe and $^{137}$Ba with one neutron hole, and four and six valence protons outside the $Z = 50$ closed shell, respectively. Detailed data on the low-spin states in $^{135}$Xe were obtained in $\beta$-decay studies of $^{135}$I [13,14]. The $11/2^-$ neutron-hole isomer at 526.551(13) keV with a half-life of 15.29(5) min [15] has been known since the 1940s [16,17]. First results on the high-spin structure were obtained by Fotiades *et al.* [18] in 2007, who measured $^{135}$Xe as a fusion-fission fragment from the $^{226}$Th compound nucleus via triple-$\gamma$ coincidences using the GAMMASPHERE array at Lawrence Berkeley National Laboratory (LBNL). The level scheme was extended up to 3.17 MeV in energy. Tentative spin-parity assignments were given up to the 2058-keV level. High-spin isomers were not subjects of the experiment.

The data on low-spin states of the stable isotope $^{137}$Ba originate from earlier work utilizing $\beta$ decay [19,20], neutron-induced reactions [21], and Coulomb excitation [22]. The spins and parities of the ground state and the $11/2^-$ isomer at 661.659(3) keV with a half-life of 2.552(1) min are well established [23]; the 661.657(3)-keV $M4$ $\gamma$-ray transition is even one of the best-known energy calibration standards in nuclear physics. The decay of this $\nu h_{11/2}^{-1}$ state attracted renewed attention with the recent observation of both a competitive $E5$ decay [24] and double-$\gamma$ decay [25]. A pioneering work on medium-spin states was performed by Kerek *et al.* in 1973 [26]. The authors irradiated a $^{136}$Xe-enriched gas target with 20–29 MeV $\alpha$ particles to populate $^{137}$Ba. Excited states were observed up to excitation energies of approx. 3 MeV, among them the $T_{1/2} = 590(10)$ ns isomeric state at 2349.1 keV with possible spin assignments $J^\pi = (15/2, 17/2, 19/2)$. This state was found to decay via a cascade of 120.2- and 1567.3-keV $\gamma$ rays, finally populating the long-lived $11/2^-$ isomer. A 274.7-keV $\gamma$-ray decay was observed to connect another higher-lying nonisomeric 2623.8-keV state with the 2349.1-keV isomeric state. The half-life of this 2623.8-keV state was constrained to be smaller than 70 ps.

Low-lying $J^\pi = 11/2^-$ yrast-trap isomers are a common and unifying feature of even-odd nuclei along the $N = 81$ isotone chain ranging from $^{131}$Sn up to $^{151}$Yb. These states correspond to one-neutron hole in the $h_{11/2}$ orbital and decay predominantly via $M4$ $\gamma$-ray transitions to the positive-parity $d_{3/2}$ ground states or the first excited $3/2^+$ states [35,36]. Another characteristic nuclear-structure feature along the lower-mass $N = 81$ isotones are shorter-lived high-spin isomers above the $11/2^-$ states. A compilation of several partial level schemes is shown in Fig. 1. Besides the aforementioned $J = (15/2, 17/2, 19/2)$ 0.6-$\mu$s isomer at 2.349 MeV in $^{137}_{56}$Ba, high-spin isomers were also found in $^{133}_{52}$Te and $^{139}_{58}$Ce. The level scheme of $^{133}$Te was extended up to 6.2 MeV with tentative spin assignments up to $J^\pi = (31/2^-)$ [30]. A $J^\pi = (19/2^-)$ state at 1.610 MeV was found to be isomeric with an adopted half-life of $T_{1/2} = 100(5)$ ns [37]. The level scheme of $^{139}$Ce is known up to 8.0 MeV in excitation energy and $43/2^-$ in spin [31,38]. The half-life of the first $J^\pi = 19/2^-$ state at 2.632 MeV was observed to be $T_{1/2} = 70(5)$ ns [39]. A $[\nu h_{11/2}^{-1} \otimes |4^+; {}^{140}\mathrm{Ce}\rangle]$ configuration was assigned via $g$-factor measurements [40]. The most elaborate nuclear structure information along the $N = 81$ isotone chain is available for $^{141}$Nd. Recently, the level scheme was extended up to an excitation energy of 18.9 MeV and spin $(81/2)\hbar$ [32,41]. Several dipole and quadrupole bands above 4.4 MeV were discovered. The dipole bands were interpreted as magnetic rotational bands, with transition probabilities that show the characteristic decrease with angular momentum caused by the shears mechanism. Furthermore, they exhibit a shape evolution from low-deformation triaxial to spherical shape. In an earlier $(\alpha, 5n\gamma)$ experiment, delayed time distributions were measured for the 349-keV $17/2^- \rightarrow 15/2^-$ and the 1781-keV $15/2^- \rightarrow 11/2^-$ transitions depopulating the 2886-keV level. An isomeric state with $T_{1/2} = 26(5)$ ns was deduced to be located at an energy of $2886 + x$ keV [33]. However, this isomer was not confirmed by the later studies in Refs. [32,41]. Thus, the typical feature of $J^\pi = 19/2^-$ isomers is first discontinued in $^{141}$Nd. In $^{143}$Sm (cf. Fig. 1) a $J^\pi = 23/2^{(-)}$

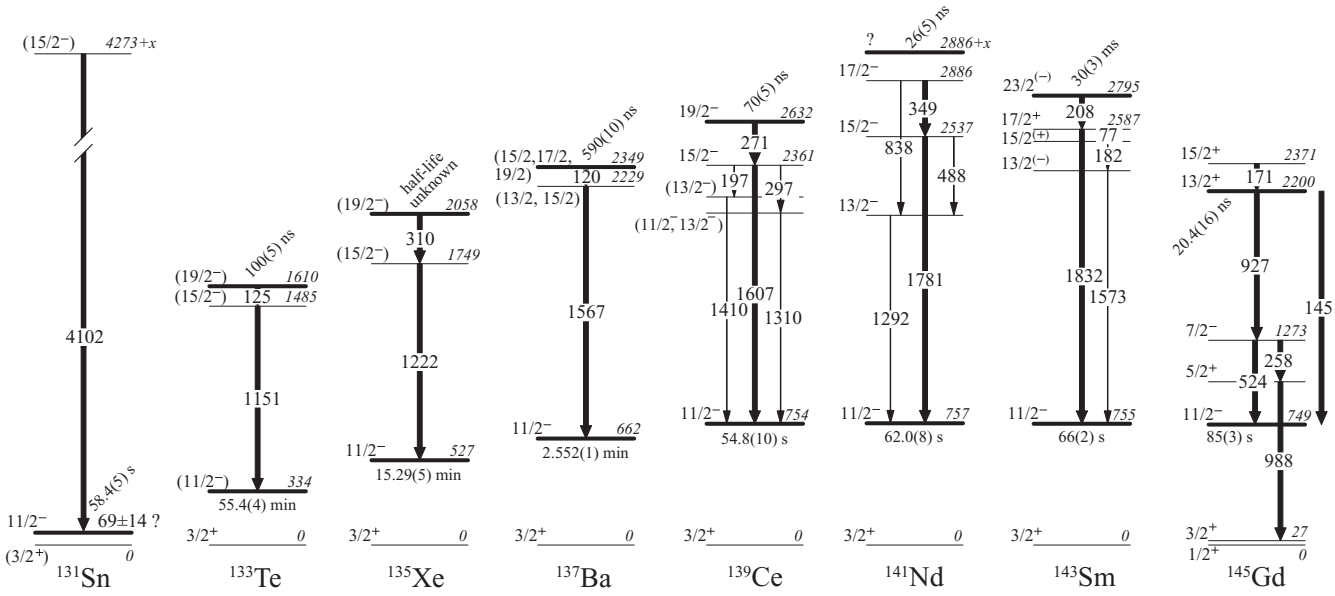


FIG. 1. Comparison of high-spin states and isomer half-lives along the $N = 81$ isotones; data taken from Refs. [18,26–34]. A sequence of $J^\pi = 19/2^-$ isomers is found in the isotones ranging from $^{133}$Te to $^{139}$Ce. Tentative assignments are written in parentheses.

isomer with a half-life of 30(3) ms is located at 2795 keV [42]. The level scheme is known up to 12 MeV with spin $(57/2)^-$. The 2795-keV isomer is explained as a three-quasiparticle $[\nu h_{11/2}^{-1} \otimes \pi(g_{7/2}^{-1} d_{5/2}^{-1})_{6^+}]$ configuration [43]. Again, the high-spin structure evolves by adding two more protons with respect to the $^{143}$Sm nucleus. In $^{145}$Gd, a 2200-keV $13/2^+$ isomer with a half-life of 20.4(16) ns decays predominantly by a strongly collective $E3$ transition to the $7/2^-$ state. The $13/2^+$ state is proposed to be a mixing of the one-phonon $[\nu 1 f_{7/2} \otimes |3^-; {}^{146}\mathrm{Gd}\rangle]$ and the $\nu 0 i_{13/2}$ configurations [34,42]

A significant piece of experimental information is missing for two nuclei along the presented $N = 81$ isotonic chain, namely $^{135}$Xe and $^{137}$Ba. The available data concern either low-spin levels observed in single-nucleon transfer reactions or levels with spin values limited by the $\beta^-$-decay selection rules. The existing data on the states above the $11/2^-$ isomers in $^{135}$Xe and $^{137}$Ba are rather scarce and the spin-parity assignments of the known levels are only tentative. The lifetime of the expected $J^\pi = (19/2^-)$ isomer in $^{135}$Xe is unknown. The limited experimental data, together with recent theoretical advances, motivate a refined investigation of nuclear-structure features in both nuclei and a test of the predictive power of modern shell-model calculations.

In this article, we report and discuss new results for $^{135}$Xe and $^{137}$Ba obtained in four different experiments. Two of these experiments were based on direct identification of the nuclei of interest and coincident prompt $\gamma$-ray spectroscopy. The combination of the high-resolution position-sensitive Advanced Gamma Tracking Array (AGATA) [44] and the PRISMA magnetic mass spectrometer [45–47] was employed to study the nuclei after $^{136}$Xe + $^{208}$Pb multinucleon-transfer (MNT) and $^{136}$Xe + $^{238}$U MNT and fission reactions, respectively. Another experiment to study both nuclei of interest was conducted at the GAMMASPHERE+CHICO setup [48,49] at Lawrence Berkeley National Lab (LBNL), using a $^{136}$Xe + $^{198}$Pt MNT reaction. In addition, $^{137}$Ba was populated via the fusion-evaporation reaction $^{130}$Te($^{11}$B, $p3n$) employing the High-efficiency Observatory for $\gamma$-Ray Unique Spectroscopy (HORUS) [50] at the Institute of Nuclear Physics, University of Cologne.

This paper is organized as follows: the experimental setup and data analysis of the four experiments are described in Sec. II, followed by the experimental results in Sec. III. A detailed comparison with shell-model calculations is presented in Sec. IV before the paper closes with a summary and conclusions.

## II. EXPERIMENTAL PROCEDURE AND DATA ANALYSIS

The $^{136}$Xe + $^{238}$U and $^{136}$Xe + $^{208}$Pb MNT experiments, performed at the Laboratori Nazionali di Legnaro at beam energies of 7.35 and 6.84 MeV/nucleon, respectively, delivered an isotopic identification of the nuclei of interest. Correlations between prompt $\gamma$-ray transitions populating isomers and delayed deexciting $\gamma$-ray transitions were enabled by the pulsed-beam $^{136}$Xe + $^{198}$Pt experiment employing the GAMMASPHERE+CHICO setup at LBNL. Furthermore, $^{137}$Ba was populated via the fusion-evaporation reaction $^{130}$Te($^{11}$B, $p3n$) with a beam energy of 54 MeV at the FN Tandem accelerator of the Institute of Nuclear Physics, University of Cologne, providing detailed $\gamma\gamma$-coincidence data. Details of the four complementary experiments are described below.

### A. $^{136}$Xe + $^{238}$U

The PIAVE+ALPI accelerator complex at the Laboratori Nazionali di Legnaro provided a $^{136}$Xe beam with an energy of 1 GeV and a beam current of 2 pnA. The beam was used to subsequently bombard two different $^{238}$U targets with thicknesses of 1 and 2 mg/cm$^2$. A 0.8-mg/cm$^2$ Nb backing faced the beam. The light projectile-like reaction fragments were identified

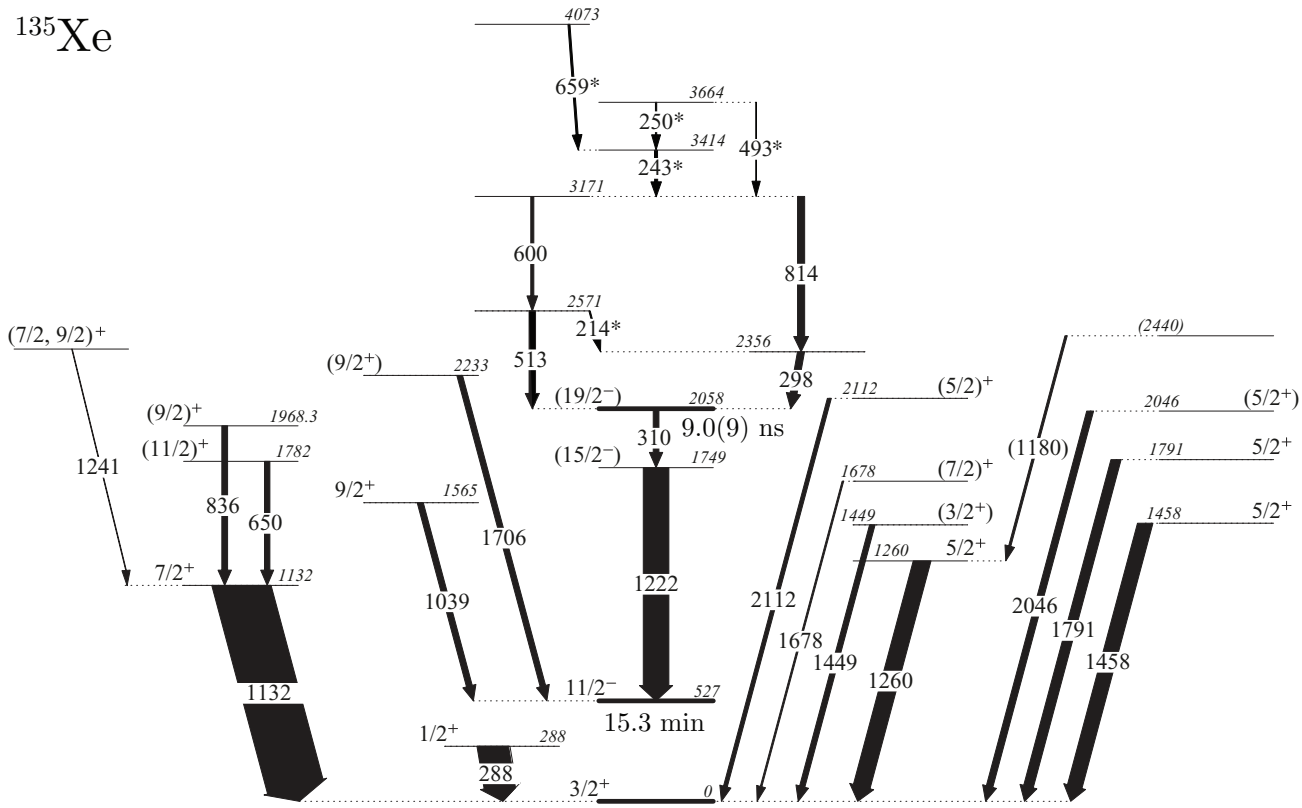


FIG. 2. Level scheme of $^{135}$Xe with the newly observed 214-, 243-, 250-, 493-, and 659-keV $\gamma$-ray transitions marked with an asterisk. Spins and parities of the states below 2.3 MeV are taken from Refs. [13,15,18]. Intensities are extracted from the $^{136}$Xe + $^{208}$Pb experiment and normalized to the 1132-keV $\gamma$-ray transition. See text for details.

with the magnetic mass spectrometer PRISMA [45–47] placed at the grazing angle of $\theta_{\text{lab}} = 50^{\circ}$. Nuclear charge, mass and the velocity vector for the individual lighter reaction products were determined via an event-by-event trajectory reconstruction within the magnetic system. $\gamma$ rays from excited states in both beam- and target-like nuclei were detected with AGATA [44] in the demonstrator configuration [51] placed 23.5 cm from the target position. The array consisted of 15 large-volume electronically segmented high-purity Ge (HPGe) detectors in five triple cryostats [52]. An event registered by the PRISMA focal-plane detector in coincidence with an AGATA event was taken as a trigger for the data acquisition. Pulse-shape analysis of the digitized detector signals was applied to determine the individual interaction points [53]. This information is used by the Orsay forward-tracking algorithm [54] to reconstruct the individual emitted $\gamma$-ray energies, to determine the first interaction point of the $\gamma$ ray in the germanium and, thus, the emission angle. Combining this information with the kinematic information of PRISMA, a precise Doppler correction for beam- and target-like nuclei was performed. Further details on the analysis are available in Ref. [55].

### B. $^{136}$Xe + $^{208}$Pb

In this experiment, a $^{136}$Xe beam from the PIAVE+ALPI accelerator complex at an energy of 930 MeV impinged onto a 1-mg/cm$^2$-thick $^{208}$Pb target. PRISMA was placed at the grazing angle of $\theta_{\text{lab}} = 42^{\circ}$. $\gamma$ rays were measured by the AGATA Demonstrator in a configuration of three triple clusters. The further setup, trigger conditions, and the data analysis are similar to those described in Sec. II A. The measurement of the momentum vector of beam-like recoils with PRISMA enabled a reconstruction of the total kinetic energy loss (TKEL) value of the reaction which is defined as the energy transferred to internal degrees of freedom and corresponds to the reaction's $Q$ value with an opposite sign [46,56]. Further details on the analysis can be found in Refs. [57,58].

### C. $^{136}$Xe + $^{198}$Pt

A 850-MeV $^{136}$Xe beam provided by the 88-Inch Cyclotron impinged onto a self-supporting 420-$\mu$g/cm$^2$ $^{198}$Pt target, isotopically enriched to >92%. $\gamma$ rays were detected by the GAMMASPHERE array, which in this experiment consisted of 103 Compton-suppressed HPGe detectors [48]. Both polar and azimuthal angles and the time-of-flight difference $\Delta t_{\text{TOF}}$ between the detection of beam-like and target-like reaction products were measured with the gas-filled parallel-plate avalanche detector array CHICO, allowing for an event-by-event Doppler-shift correction for emitted $\gamma$ rays. The experimental trigger required two CHICO elements and at least three germanium detectors to fire. Further details are given in Ref. [59]. The data from the experiment were sorted into four two-dimensional matrices gated on beam-like fragments: (i) an in-beam Doppler-corrected prompt $\gamma\gamma$ matrix, (ii) an out-of-beam delayed-delayed $\gamma\gamma$ matrix, (iii) a

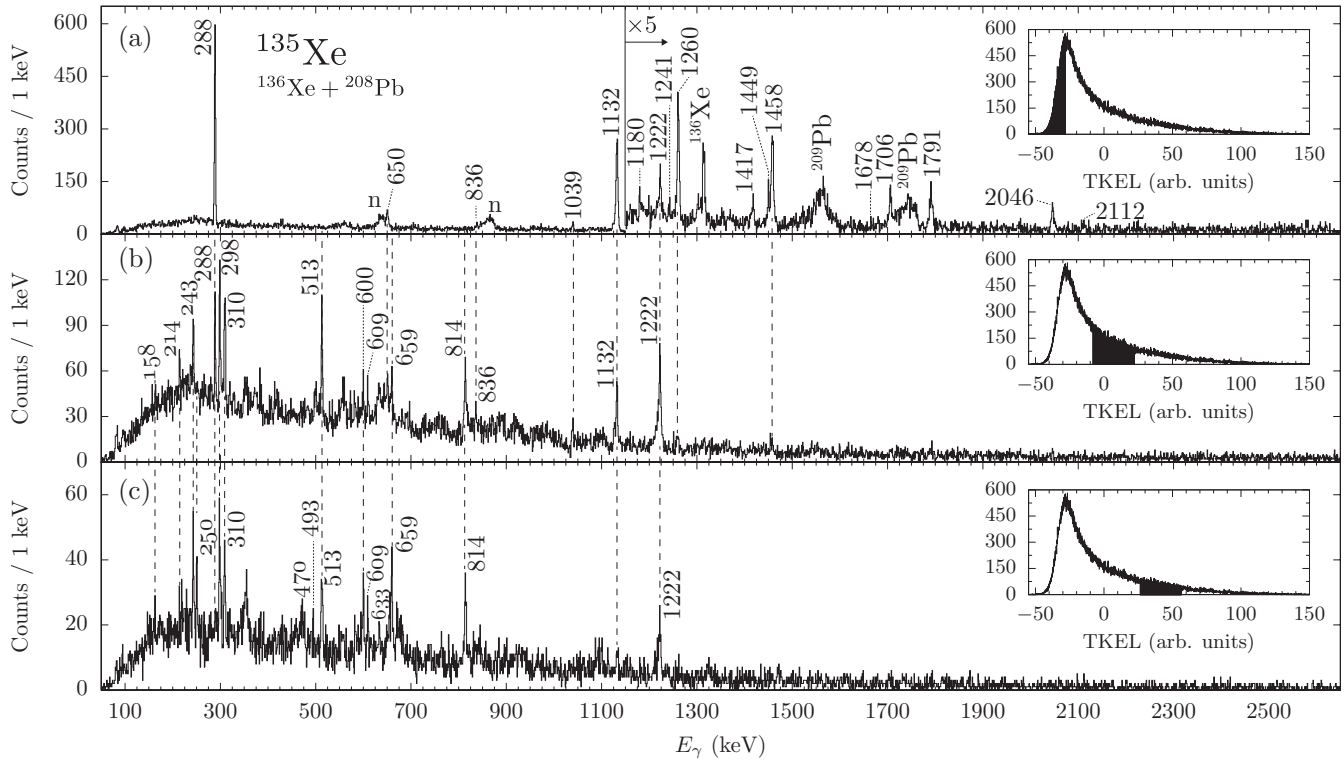


FIG. 3. Doppler-corrected $^{135}$Xe $\gamma$-ray spectra from the $^{136}$Xe + $^{208}$Pb experiment: (a) Gate on low TKEL, (b) gate on intermediate TKEL, and (c) gate on large TKEL corresponding to higher excitation energies after the deep-inelastic MNT reaction. The applied gates on the TKEL distributions are shown in the three insets, respectively. The main peaks of the TKEL distributions are shifted to negative values due to large energy losses in the thick Pb targets. A gate on the prompt time peak between AGATA and PRISMA is applied to all spectra.

delayed-prompt $\gamma\gamma$ matrix, and (iv) a delayed-$\gamma$-time matrix for extracting isomeric decay half-lives. The time window for the delayed $\gamma$ rays was set from 45 to 780 ns. The RADWARE analysis package [60] was used to project and background-subtract the gated spectra.

### D. $^{11}$B + $^{130}$Te

In a fourth experiment, $^{137}$Ba was populated via the fusion-evaporation reaction $^{130}$Te($^{11}$B, $p3n$)$^{137}$Ba, employing a 54 MeV $^{11}$B beam delivered by the FN Tandem accelerator of the Institute of Nuclear Physics, University of Cologne. The 99.3% enriched $^{130}$Te target with a thickness of 1.8 mg/cm$^3$ was evaporated onto a 120 mg/cm$^3$ thick Bi backing plus a 132 mg/cm$^3$ thick Cu layer for heat dissipation. All residual reaction products are stopped inside the Bi backing. The reaction codes PACE4 [61] and CASCADE [62] predict a relative cross section of approx. 0.8% for the population of the p3n channel at this beam energy. $\gamma$ rays from excited states were measured employing the HORUS array [50] comprising 14 HPGe detectors, six of them equipped with BGO Compton-suppression shields. The detectors are positioned on the eight corners and six faces of a cube geometry. Evaporated charged particles were detected with a double-sided silicon strip detector mounted at backward direction covering an angular range from 118° to 163°. The count rate of the individual HPGe crystals was maintained around 20 kHz during the experiment. $\gamma\gamma$ coincidences were processed and recorded utilizing the synchronized 80 MHz XIA Digital Gamma Finder (DGF) data-acquisition system. The data were sorted into various two- and three-dimensional matrices with a time gate of 250 ns using the SOCO-V2 code [63]. In total, $1.5 \times 10^{10}$ $\gamma\gamma$ and $8.0 \times 10^9$ $\gamma\gamma\gamma$ coincidence events were collected. The analysis was performed with the program TV [64].

## III. RESULTS

### A. $^{135}$Xe

The level scheme of $^{135}$Xe deduced in the present work is presented in Fig. 2. Ejectile Doppler-corrected singles $\gamma$-ray spectra of $^{135}$Xe produced in the $^{136}$Xe + $^{208}$Pb experiment are shown in Fig. 3 with gates on (a) low, (b) intermediate, and (c) large total kinetic energy losses (TKEL). The applied gates on the TKEL distributions are shown in the three insets and are marked in black. Gates on the TKEL distributions restrict the total excitation energy of the reaction system. In particular, events with small TKEL values are related to reaction products with a lower excitation energy. Thus, by correlating the TKEL distributions with coincident $\gamma$ rays of AGATA, $\gamma$-ray transitions between states with different excitation energies and angular momenta can be suppressed or enhanced [46,65]. $^{135}$Xe is produced by a one-neutron stripping reaction; therefore, a multitude of low-lying excited states with spins $J < 11/2\hbar$ are populated with a gate on low TKEL, cf. Figs. 3(a) and 2. In contrast, $\gamma$-ray spectra with gates on larger TKEL show prominent $\gamma$ rays with energies of

TABLE I. Energies, assignments and relative in-beam intensities for transitions observed in $^{135}$Xe above the $11/2^-$ isomer. Fitted energies and intensities normalized to the 1222-keV transition are taken from the $^{136}$Xe + $^{208}$Pb AGATA experiment.

| $E_\gamma$ (keV) | $E_i$ (keV) | $E_f$ (keV) | $I_i^\pi$ | $I_f^\pi$ | $I_\gamma$ |
|---|---|---|---|---|---|
| 158 | | | | | weak |
| 214 | 2571 | 2356 | | | 5(2) |
| 243 | 3414 | 3171 | | | 12(2) |
| 250 | 3664 | 3414 | | | 6(2) |
| 298 | 2356 | 2058 | | $(19/2^-)$ | 26(2) |
| 310 | 2058 | 1749 | $(19/2^-)$ | $(15/2^-)$ | 22(2) |
| 470 | | | | | weak |
| 493 | 3664 | 3171 | | | weak |
| 513 | 2571 | 2058 | | $(19/2^-)$ | 24(2) |
| 600 | 3171 | 2571 | | | 12(3) |
| 609 | | | | | 9(2) |
| 633 | | | | | weak |
| 659 | 4073 | 3414 | | | 3(1) |
| 814 | 3171 | 2356 | | | 28(3) |
| 1222 | 1749 | 527 | $(15/2^-)$ | $11/2^-$ | ≡100 |

298, 310, 513, 600, 814, and 1222 keV that were reported by Fotiades *et al.* [18] to be transitions depopulating medium-spin states above the $11/2^-$ isomer. New $\gamma$ rays identified in the present work with energies of 158, 214, 243, 250, 470, 493, 609, 633, and 659 keV are labeled in italic characters in Fig. 3 and summarized in Table I. Intensities are taken from the $^{136}$Xe + $^{208}$Pb experiment. Various GAMMASPHERE prompt $\gamma\gamma$-coincidence spectra are shown in Figs. 4(a) to 4(g). Coincidences are marked with arrows. Some spectra are over-subtracted due to considerable nonuniform background contributions by falsely Doppler-corrected target excitations.

The placement of the 298-, 513-, 600-, and 814-keV transitions by Fotiades *et al.* is verified; the 298–814- and 513–600-keV cascades are mutually coincident. Their placement above the 2058-keV state is also consistent with the TKEL-gated AGATA spectra: The 1222-keV line is already visible for low TKEL in Fig. 3(a), while the 310-keV and the four aforementioned transitions first appear for intermediate TKEL values. The 214-keV $\gamma$ ray fits the energy difference of the 2571- and 2356-keV state and emerges in the intermediate-TKEL gated spectrum in Fig. 3(b). Furthermore, it is mutually coincident with the 298-keV transition as shown in Figs. 4(a) and 4(g). Consequently, the transition is placed between the two states. The 243-keV $\gamma$-ray transition first appears in Fig. 3(b) with a gate on intermediate TKEL; the 250- and 493-keV $\gamma$-ray transitions are only visible in panel (c) with gates on large TKEL. Moreover, the 243-keV $\gamma$ ray is coincident with all major transitions between the 2058- and 3171-keV levels and placed on top of the 3171-keV level. In accordance with the intensity balance, the 250-keV $\gamma$ ray, which is coincident with the 243-keV $\gamma$ ray, is placed directly on top. The 493-keV $\gamma$ ray corresponds to the sum energy of the two aforementioned transitions and is not coincident with either the 243- or the 250-keV transitions. Additionally, Fig. 4(f) shows that the 659-keV transition is coincident with the lines at 243, 298, and 814 keV. The transition is placed

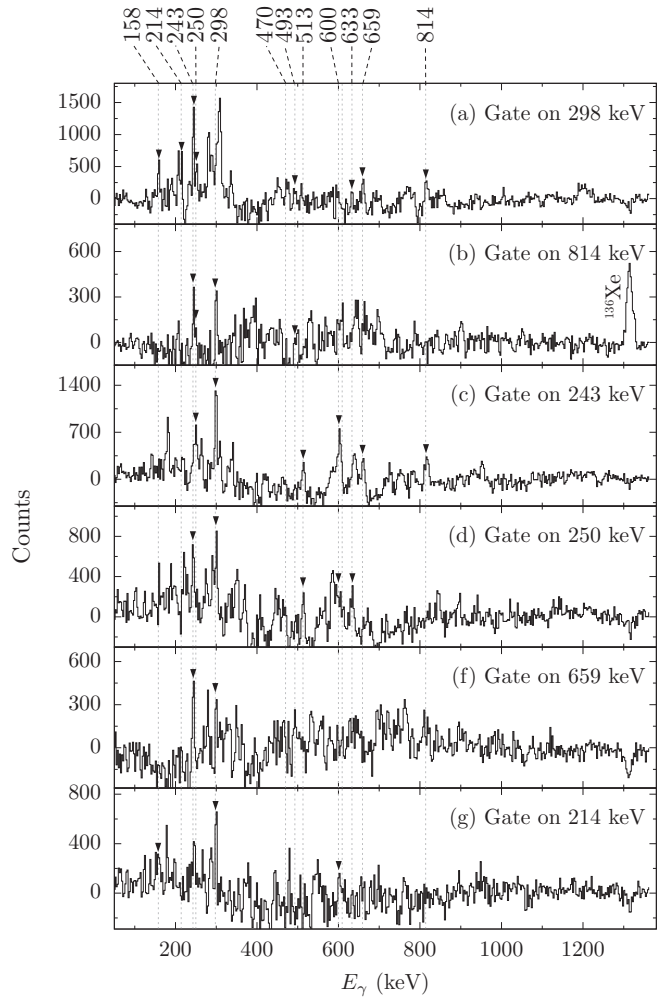


FIG. 4. GAMMASPHERE prompt $\gamma\gamma$-coincidence spectra with gates on (a) 298, (b) 814, (c) 243, (d) 250, (e) 659, and (f) 214 keV. Coincidences are labeled by arrow heads. Vertical lines corresponding to peak energies observed in $^{135}$Xe are drawn to guide the eye.

parallel to the 250-keV transition. No conclusive coincidences and placements are found for the 158-, 470-, 609-, and 633-keV $\gamma$ rays.

The systematics along the $N = 81$ isotones ranging from $^{133}$Te to $^{139}$Ce suggests the $J^\pi = (19/2^-)$ state at 2058 keV to be of isomeric character (cf. Fig. 1 in Sec. I). Figures 5(a) and 5(b) show the GAMMASPHERE delayed out-of-beam $\gamma$-ray spectra gated by 310 and 1222 keV. Both delayed transitions are mutually coincident with low peak intensities. However, both 310- and 1222-keV transitions depopulating the 2058 keV level are also clearly observed in the prompt AGATA $\gamma$-ray spectra. Thus, the lifetime of the 2058-keV state has to be of the order of the width of the prompt peak in the time-difference spectrum between PRISMA and AGATA, i.e. $\Delta t_{\text{PRISMA-AGATA}} \approx 16$ ns. The precise lifetime is determined using the GAMMASPHERE $\gamma$-time matrix. The 1222-keV peak is contaminated by the delayed 1220.1-keV $11/2^- \rightarrow 7/2^-_{\text{g.s.}}$ transition which is part of the depopulating $\gamma$-ray cascade of the $19/2^-$ isomer with $T_{1/2} = 10.1(9)$ ns in $^{137}$Xe [23]. Nonetheless, the peak at 310 keV has an expected

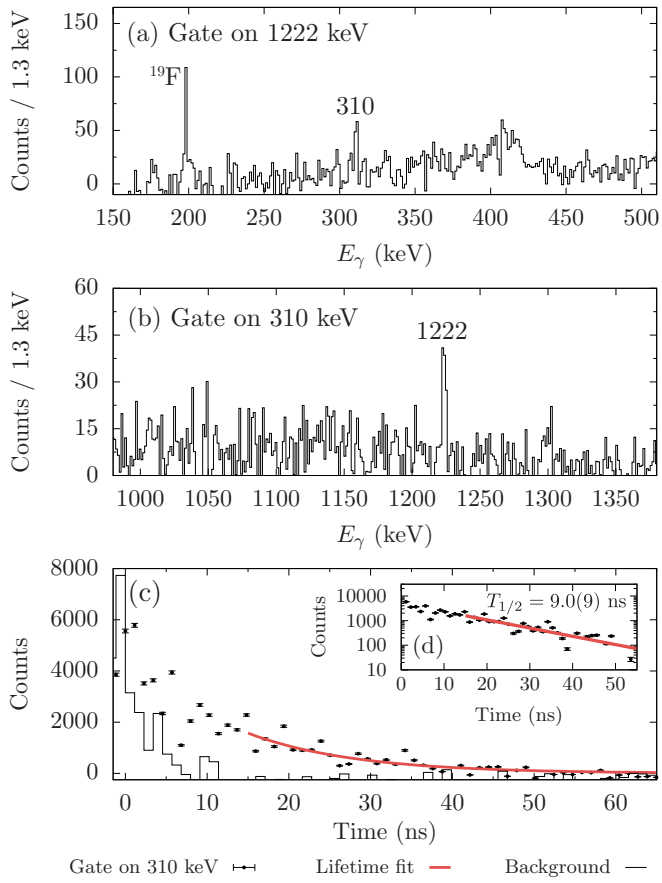


FIG. 5. (a) GAMMASPHERE delayed out-of-beam $\gamma$-ray spectrum gated by the delayed 1222-keV transition in $^{135}$Xe. (b) Same spectrum as in (a), gated on the 310-keV transition. (c) Linear GAMMASPHERE time spectrum gated by the 310-keV transition (black data points) with an exponential decay-curve fit (red solid line). A background prompt time spectrum is plotted with solid steps. (d) Same as (c), but with a logarithmic scale. The fitted half-life is $T_{1/2} = 9.0(9)$ ns.

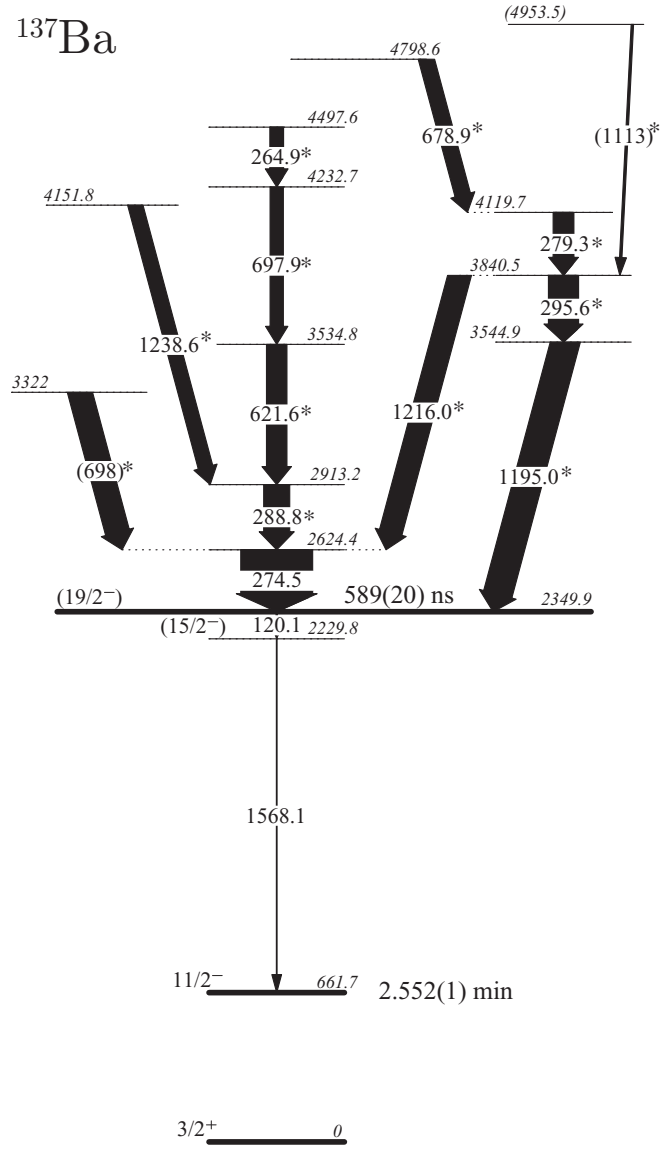


FIG. 6. Level scheme assigned to $^{137}$Ba in the present work. Transition and excitation energies are given in keV. The decay of the $11/2^-$ isomer is not observed due to its long half-life. $\gamma$-ray intensities of transitions above the 2349.9-keV isomer are deduced from the $^{11}$B + $^{130}$Te experiment and normalized to the 274.5-keV transition. Isomeric states are marked with thick lines and labeled with the corresponding half-lives. Spins and parities of the states below 2.35 MeV follow the systematics of the $N = 81$ isotonic chain. New $\gamma$-ray transitions are marked with an asterisk. See text for details.

FWHM of 1.5 keV and shows no sign of contamination. The corresponding background-subtracted time projection (black points) and the fitted decay curve (solid line) are shown in Fig. 5(c). A time spectrum of a nearby background region around 307 keV is plotted with solid steps. Any residual background of the prompt peak in the time spectrum is negligible for the decay-curve fit. The fit function of the time spectrum $N(t)$ is chosen as $N(t) = a \exp[t \ln(2)/T_{1/2}] + b$. The background parameter $b$ is fitted between 200 and 780 ns and held constant in the decay-curve fit. The fitted half-life is 9.0(9) ns for the 2058-keV state.

### B. $^{137}$Ba

The level scheme of $^{137}$Ba deduced in this work is presented in Fig. 6. Corresponding $\gamma$-ray transitions are summarized in Table II. The intermediate-spin region below the long-lived $(19/2^-)$ isomer is accessible by utilizing delayed-delayed as well as delayed-prompt coincidences from the GAMMASPHERE+CHICO dataset. Figure 7(a) presents the delayed $\gamma$-ray spectrum with a gate on the delayed 120-keV transition. The spectrum shows the expected prominent peak at 1568 keV. Some contaminant peaks are caused by the nearby delayed 121-keV $(10^+) \rightarrow (8^+)$ transition in $^{134}$Ba [66]. The gate on the 1568-keV $\gamma$-ray transition, which directly feeds the $11/2^-$ isomer, shows a distinct peak at 120 keV in Fig. 7(b). Intense peaks at 110 and 197 keV in the spectra originate from the $\gamma$-ray decay of long-lived excited states which were populated in $^{19}$F$(n,n'\gamma)$ reactions of neutrons evaporated after MNT with fluorine present in Teflon® tapes

TABLE II. Energies, assignments and relative in-beam intensities for transitions observed in $^{137}$Ba above the $11/2^-$ isomer. Fitted energies and intensities normalized to the 274.5-keV transition are taken from the $^{11}$B + $^{130}$Te HORUS experiment. The uncertainties in the transition energies are ±0.5 keV. Possible spin/parity assignments are discussed in Sec. IV.

| $E_\gamma$ (keV) | $E_i$ (keV) | $E_f$ (keV) | $I_i^\pi$ | $I_f^\pi$ | $I_\gamma$ |
|---|---|---|---|---|---|
| 120.1 | 2349.9 | 2229.8 | $(19/2^-)$ | $(15/2^-)$ | |
| 245 | | ⩾3840.5 | | | 10(3) |
| 264.9 | 4497.6 | 4232.7 | | | 19(2) |
| 274.5 | 2624.4 | 2349.9 | $(21/2^-)$ | $(19/2^-)$ | ≡100 |
| 279.6 | 4119.7 | 3840.5 | | | 29(3) |
| 288.8 | 2913.2 | 2624.4 | | | 38(7) |
| 295.6 | 3840.5 | 3544.9 | | | 43(7) |
| 621.6 | 3534.8 | 2913.2 | | | 30(3) |
| 678.9 | 4798.6 | 4119.7 | | | 23(4) |
| 697.9 | 4232.7 | 3534.8 | | | 20(5) |
| 780 | | ⩾3840.5 | | | 10(4) |
| 1113 | (4953.5) | (3840.5) | | | 4(2) |
| 1195.0 | 3544.9 | 2349.9 | | $(19/2^-)$ | 43(8) |
| 1216.0 | 3840.5 | 2624.4 | | | 34(3) |
| 1238.6 | 4151.8 | 2913.2 | | | 22(6) |
| 1568.2 | 2229.8 | 661.7 | $(15/2^-)$ | $11/2^-$ | |

within the HPGe detector configuration. As no significant contamination of other delayed $\gamma$ rays is present in the 1568-keV gated spectrum, the $\gamma$-time matrix is exploited for this transition. The inset in Fig. 7(b), marked as 7(c), shows the corresponding decay curve obtained by a gate on the delayed 1568-keV transition. Fits are performed for six different time windows between 100 ns and 700 ns. The half-life of the 2349.9-keV excited state is determined to be 589(20) ns using the weighted arithmetic mean of the individual fits. It is in good agreement with the previously measured value of 590(10) ns [26]. No evidence is found for further few-ns lifetimes above the 2349.9-keV state.

A gate on the GAMMASPHERE delayed 1568-keV transition is applied to generate the prompt $\gamma$-ray spectrum shown in Fig. 7(d) that contains the transitions feeding the 2349.9-keV isomer. A series of densely located peaks stands out around the dominating 275-keV peak which was already reported by Kerek *et al.* [26]. Fifteen of the 23 transition candidates visible in the delayed-prompt $\gamma$-ray spectrum are also present in the ejectile Doppler-corrected singles $\gamma$-ray spectrum of the $^{136}$Xe + $^{238}$U AGATA experiment in Fig. 8(a). The improved energy resolution of the AGATA array allows a clear separation of the closely lying lines of the GAMMASPHERE data set. The spectrum is corrected for remaining contaminations of the nearby isobar $^{137}$Cs [8] by subtracting the corresponding normalized mass-gated $\gamma$-ray spectrum. A smoothed background spectrum including Compton steps is modeled and subsequently subtracted. The corresponding PRISMA mass spectrum along the Ba isotopes is depicted in the inset (b). Random background is significantly suppressed by gating on the prompt time-difference peak between AGATA and PRISMA. In total, the $\gamma$-ray spectrum features 24 peaks; 23 of them were previously unknown. The excitation pattern of $^{137}$Ba is different compared to that of $^{135}$Xe as more nucleons are transferred. None of the known low-spin positive-parity excited states [23] are observed. Therefore, all new levels and their transitions have to be placed above the 2349.9-keV isomer.

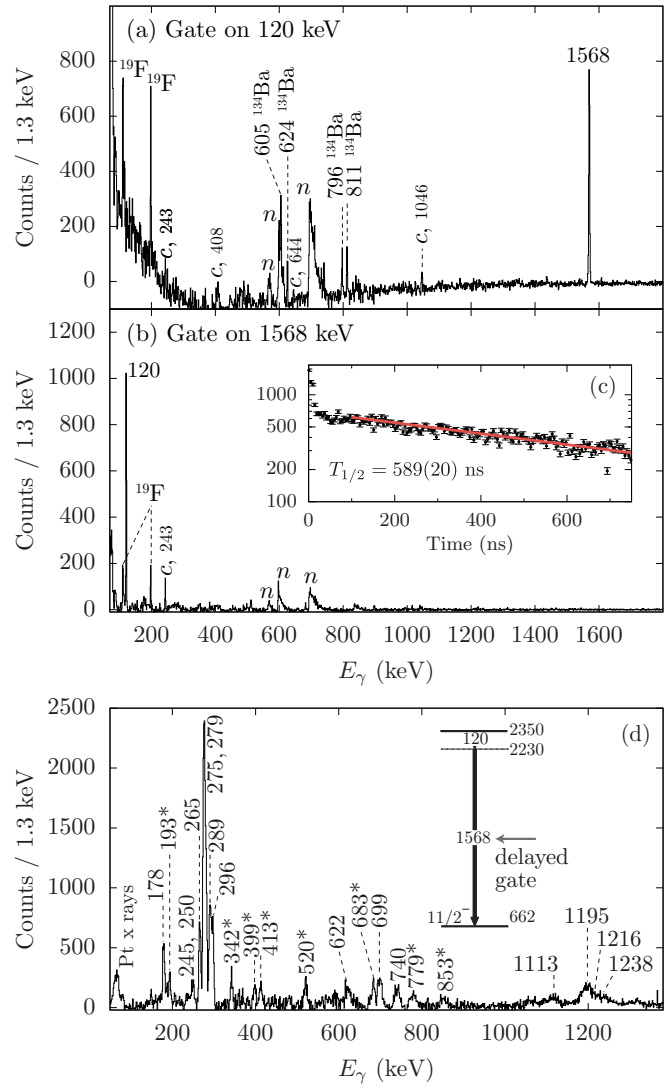


FIG. 7. (a) GAMMASPHERE delayed out-of-beam $\gamma$-ray spectrum gated by the delayed 120-keV transition in $^{137}$Ba. Contaminants from $^{134}$Ba are labeled in the spectrum. Contaminants are marked with $c$; Ge($n$,$n'\gamma$) edges with $n$. (b) Same spectrum as in (a), gated on the 1568-keV transition; no major contaminants are visible. (c) Time spectrum gated by the 1568-keV transition (data points) from which the decay curve (solid line) is obtained with a half-life of $T_{1/2}$ = 589(20) ns. (d) GAMMASPHERE delayed-prompt $\gamma\gamma$-coincidence spectrum with a gate on the delayed 1568-keV transition (partial level scheme shown in the inset). The spectrum contains prompt transitions feeding the 2349.9-keV isomer.

Both $\gamma\gamma$-double and $\gamma\gamma\gamma$-triple coincidences are exploited in the analysis of the Cologne fusion-evaporation experiment. Various HORUS prompt $\gamma\gamma$-coincidence spectra are shown in Figs. 9(a) to 9(e). Coincidences are marked in the spectra. We note that no mass identification was performed in the LBNL and Cologne experiments. Thus, only transitions

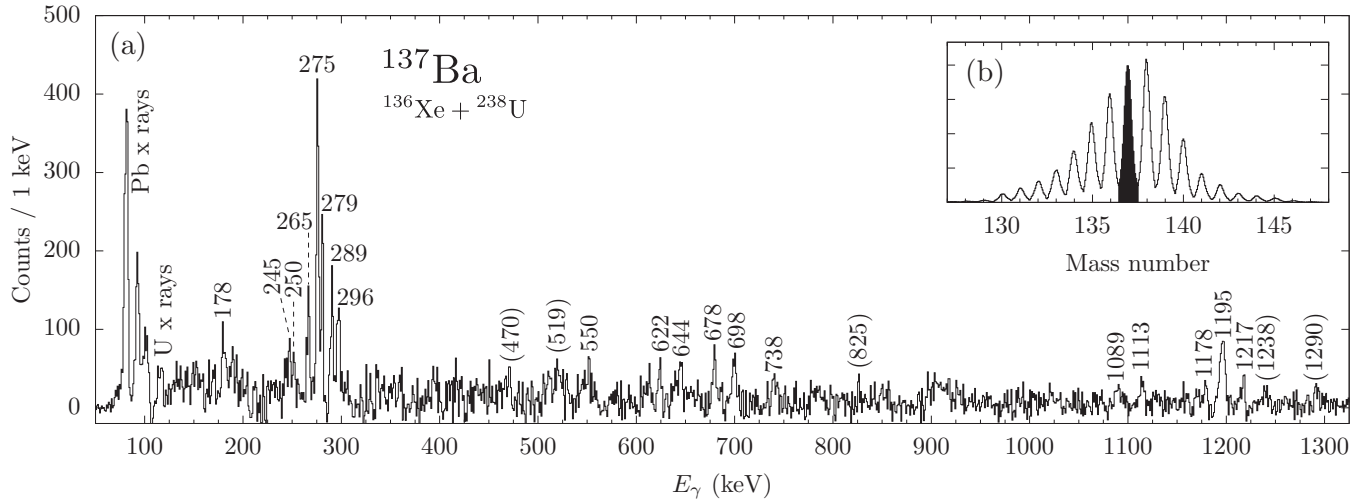


FIG. 8. (a) $^{137}$Ba ejectile Doppler-corrected $\gamma$-ray spectrum, corrected for contamination of the isobar $^{137}$Cs by subtracting the corresponding normalized mass-gated $\gamma$-ray spectra. Random background is subtracted with a gate on the prompt peak in the spectrum of time differences between AGATA and PRISMA. Only the 275-keV $\gamma$ ray was previously known. (b) Mass spectrum of the Ba isotopes obtained with PRISMA. The applied mass gate on $^{137}$Ba is marked in black.

identified in the AGATA singles spectrum (see Fig. 8) and the GAMMASPHERE delayed-prompt coincidence spectrum are considered in order to construct the level scheme above the 2349.9 keV isomer. $\gamma$-ray energies and intensities, normalized to the intensity of the 274.5-keV $\gamma$-ray transition, are listed in Table II.

The 274.5-keV transition is observed to be the most intense one and was already known to directly feed the 2349.9-keV isomer [26]. $\gamma$ rays with energies of 288.8, 621.6, 698, and 265.9 keV are mutually coincident with the 274.5-keV transition and constitute a cascade feeding the 2624.4-keV state. A 1238.6-keV $\gamma$ ray is observed to be coincident with

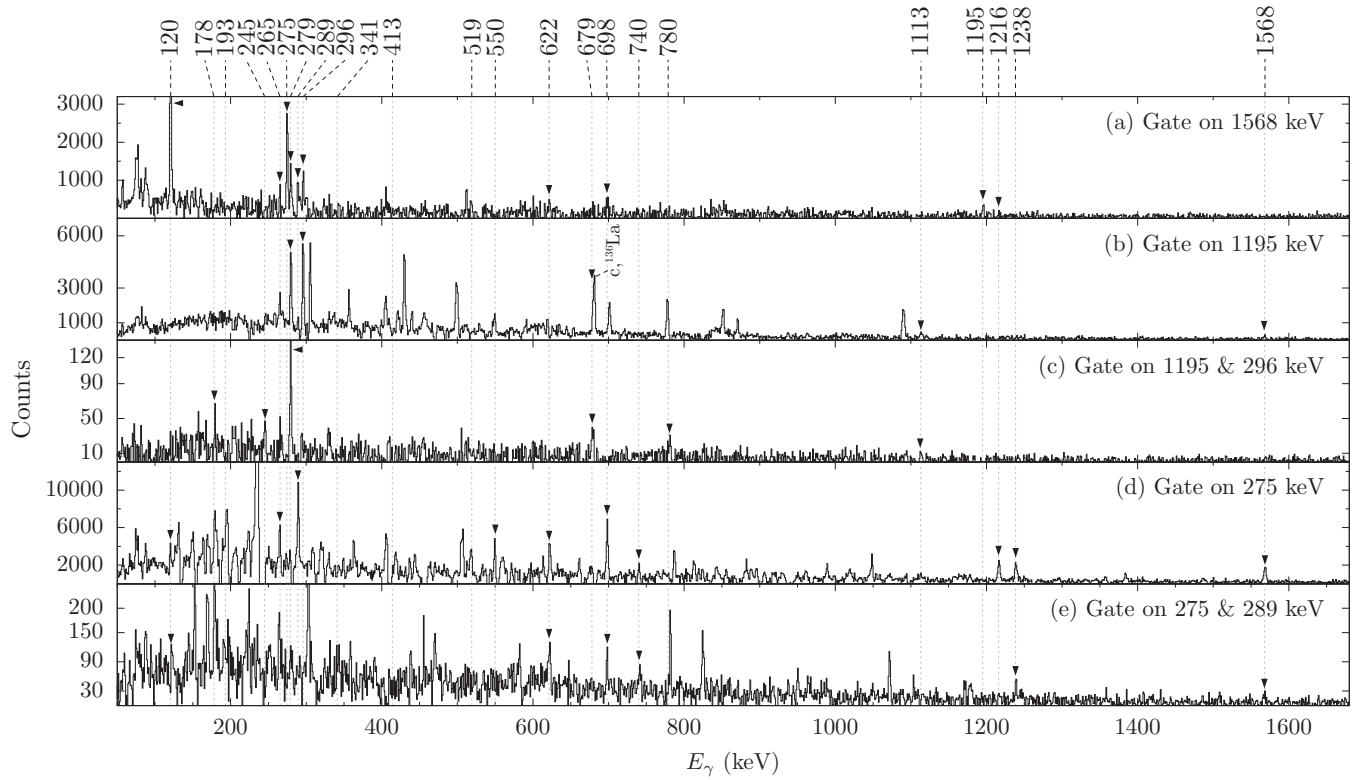


FIG. 9. Prompt HORUS $\gamma\gamma$ double- and $\gamma\gamma\gamma$ triple-coincidence spectra with gates on (a) 1568, (b) 1195, (c) 1195 & 296, (d) 275, (e) 275 & 289 keV. Coincidences are labeled by filled arrow heads. Thin grey lines corresponding to peak energies observed in Figs. 8 and 7(d) are drawn to guide the eye.

the 274.5- and 288.9-keV $\gamma$ rays, but not with the other transitions of the aforementioned cascade. Hence, the transition has to feed a 2913.2-keV state, decaying by the 288.9-keV transition. The intensity of the 698-keV $\gamma$ ray in the $\gamma\gamma$-coincidence spectrum gated on 274.5 keV exceeds the one of the 288.9-keV line. However, the intensity balance in the $\gamma\gamma\gamma$ projection gated on 274.5 and 288.9 keV suggests the 697.9-keV transition to be placed above the 2913.2-keV state. Hence, the line at 698 keV is in fact a doublet, as presented in Fig. 6. The ordering of the 697.9- and 264.9-keV transitions is tentative since the intensities are equal within their uncertainties.

Coincidences with the 1568.1-keV transition [see Fig. 9(a)] as well as the intensity balance require the newly-observed 1195.0-keV transition to be placed parallel to the 274.5-keV transition, directly feeding the isomer. Since the 295.6-, 279.3- and 678.9-keV lines are in mutual coincidence with the 1195.0-keV $\gamma$ ray [cf. Figs. 9(b) and 9(c)], all three transitions are placed on top of the newly established 3544.9-keV state according to their intensity balance. Peaks at 245 and 780 keV, also observed in the $^{136}$Xe + $^{198}$Pt experiment in Fig. 7(d), appear in the $\gamma\gamma\gamma$ spectrum double-gated on 1195 and 296 keV, but cannot be placed unequivocally in the level scheme. A 1216.0-keV $\gamma$ ray connects the 3840.5- and 2624.4-keV states. This placement is also supported by $\gamma\gamma$- and $\gamma\gamma\gamma$ coincidences as shown in Figs. 9(d) and 9(e). The 1113-keV transition is tentatively placed above the 3840.5-keV state. The obtained maximum excitation energy is consistent with other populated reaction channels in the present experiments [65]. Two 555.6- and 620.2-keV $\gamma$ rays that were tentatively assigned by Kerek *et al.* [26] to feed the 2624-keV state are not observed in this work. No conclusive placement is obtained for the other low-intensity transitions.

## IV. SHELL-MODEL CALCULATIONS

The extended level scheme and the features of long-lived isomers are compared to results of two different large-scale shell-model calculations for $^{135}$Xe and $^{137}$Ba. The first calculations were carried out without any truncations for positive- and negative-parity states in the jj55pn model space with the jj55pna Hamiltonian [1] (referred to as the SN100PN interaction) using the code NUSHELLX@MSU [67]. The SN100PN interaction is based on a renormalized $G$ matrix derived from the CD-Bonn nucleon-nucleon interaction [68]; single-particle energies were chosen to reproduce excited states in $^{133}$Sb and $^{131}$Sn. The model space comprises the full $gdsh$ valence space outside the $^{100}$Sn core between the magic numbers 50 and 82, including the $0g_{7/2}$, $1d_{5/2}$, $1d_{3/2}$, $2s_{1/2}$, and $0h_{11/2}$ orbitals for both protons and neutrons. The corresponding single-particle energies for the neutrons are $-10.609$, $-10.289$, $-8.717$, $-8.694$, and $-8.815$ MeV, respectively. Those for the protons are 0.807, 1.562, 3.316, 3.224, and 3.605 MeV.

An independent extensive theoretical study of nuclei around mass 130 was published by Teruya *et al.* [3]. The results include excited states and electromagnetic transition probabilities for Xe and Ba isotopes within the shell model in the $gdsh$ model space including the $0g_{7/2}$, $1d_{5/2}$, $1d_{3/2}$, $2s_{1/2}$, and $0h_{11/2}$ orbitals for both protons and neutrons. The interaction [in the following referred to as Pairing+Quadrupole-Quadrupole+Multipole for the mass region 130 (PQM130)] is composed of spherical single-particle energies and phenomenological two-body effective interactions consisting of monopole-pairing, quadrupole-pairing, and quadrupole-quadrupole terms. Further newly introduced higher-order pairing interactions are also taken into account. Single-particle energies (SPEs) were adopted from the experimental excited states of $^{133}$Sb (proton SPEs) and $^{131}$Sn (neutron SPEs) [3].

The shell-model calculations provide insight into the structure of the isomeric states and the levels built on top. Results of both calculations (middle and right panels) are compared to the experimental levels (left panel) of $^{135}$Xe in Fig. 10(a) and to the ones of $^{137}$Ba in Fig. 10(b), respectively. The states are separated into columns for the negative- and the positive-parity states. The lowest neutron-hole states with $J^\pi = 3/2^+$, $1/2^+$, and $11/2^-$ are well reproduced by both shell-model calculations for $^{135}$Xe as well as for $^{137}$Ba. In addition, the excitation energies of the first excited $7/2^+$ and $5/2^+$ states are fairly reproduced by both the PQM130 and the SN100PN interactions; however, the ordering of the states is reversed in both nuclei.

The $(15/2^-)$ and the $(19/2^-)$ states in $^{135}$Xe are well reproduced by the SN100PN interaction with deviations to lower energies of only 47 and 86 keV, respectively. The PQM130 interaction predicts both states at slightly higher energies with deviations of 138 and 173 keV. Larger discrepancies between the two calculations emerge in the high-spin regime; e.g., the prediction for the first $25/2^-$ state differs by 0.5 MeV. The 2356-keV state is interpreted as the $21/2^-$ state, as for lower spin values a dominant decay branch to the $15/2^-$ state is expected, which is not observed in this study. Accordingly, the state at 2571 keV has the possible spins $J^\pi = (21/2^-, 23/2^-)$. Positive-parity states with $J > 15/2$ are predicted by both calculations to appear at excitation energies larger than 2.8 MeV. States with spin $25/2^-$ are expected to be located at excitation energies above 3.2 MeV. In comparison with the experimental energy spectrum, neither interaction yields a conclusive assignment of states beyond 2.5 MeV.

The $11/2^-$ and the $(15/2^-)$ states in $^{137}$Ba are well reproduced by the PQM130 interaction. In contrast, the SN100PN interaction underestimates the $11/2^-$ level energy by 184 keV. The ordering of the first excited $17/2^-$ and $19/2^-$ levels is predicted differently by the two calculations. The experimental $(19/2^-)$ state is overpredicted by the PQM130 interaction, and underpredicted by the SN100PN interaction, both with an offset of 245 keV. However, the relative positions of the $(15/2^-)$ and $(19/2^-)$ states is better reproduced by the SN100PN interaction. Going to higher spins, the energy differences in the two calculations between states of same spin and parity amount for up to 1 MeV. The 2624.4-keV excited state can most likely be interpreted as the first $21/2^-$ state. Positive-parity states of similar spin are predicted by both calculations to appear only at higher energies; states with spin $J^\pi < 15/2^+$ would also decay into the $15/2^-$ state or the $11/2^-$ isomer. Moreover, the 2913.2-keV state

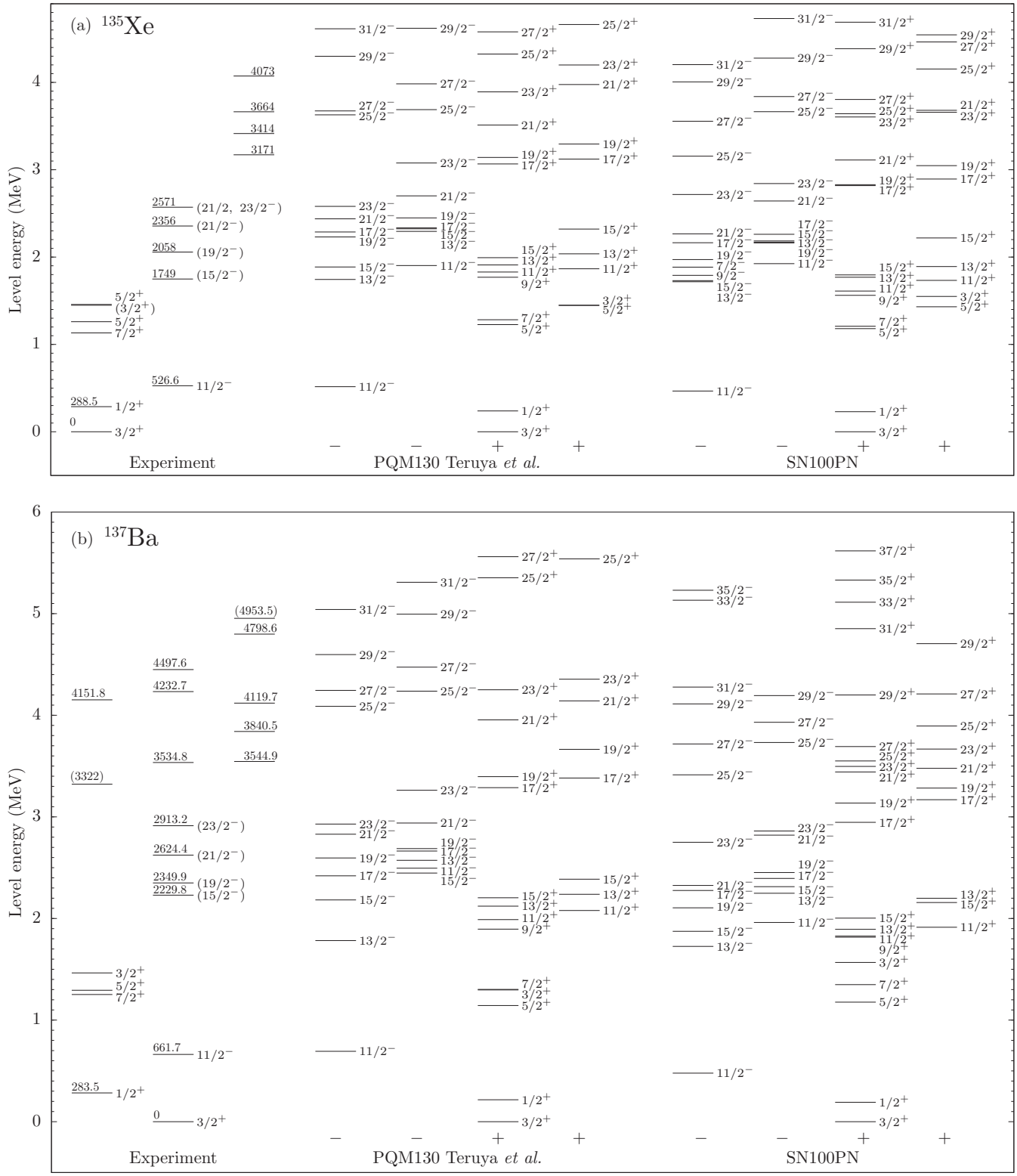


FIG. 10. Comparison of experimental energy spectra with the results of shell-model calculations for (a) $^{135}$Xe and (b) $^{137}$Ba. Experimental energy spectra are shown in the left panels. The arrangement of experimental levels for $^{137}$Ba mirrors the layout of the level scheme shown in Fig. 6. The middle panels show the results for both the first and the second excited states obtained with the PQM130 interaction [3]. The right panels show the results of the shell-model calculations within the SN100PN interaction. Note that the states are separated into columns for the negative- and the positive-parity states. The first columns contain yrast states; second columns with yrare states are added for clarity.

TABLE III. Summary of the experimental and theoretical results for $B(E2; 19/2^- \rightarrow 15/2^-)$ values of $^{133}$Te, $^{135}$Xe, and $^{137}$Ba. Experimental $\gamma$-ray transition energies are taken from Refs. [15,23,37]. The experimental results are compared to shell-model calculations employing (i) the PQM130 interaction [3] and (ii) the SN100PN interaction by Brown *et al.* [1]. In the SN100PN calculations effective neutron and proton charges are $e_\nu = 0.81e$ and $e_\pi = 1.52e$. Experimental $B(E2)$ values are corrected for internal conversion [69]. See text for details.

| A | $E_i$ (keV) | Experiment | | $J_i^\pi \rightarrow J_f^\pi$ | Theory | | | |
|---|---|---|---|---|---|---|---|---|
| | | This work / *Previous work* | | | PQM130 | | SN100PN | |
| | | $T_{1/2}$ (ns) | $B(E2)$ (W.u.) | | $E_i$ (keV) | $B(E2)$ (W.u.) | $E_i$ (keV) | $B(E2)$ (W.u.) |
| $^{133}$Te | *1610.4* | *100(5)* | *2.58(29)* | $19/2_1^- \rightarrow 15/2_1^-$ | 1798 | 2.26 | 1606 | 2.58 |
| | | | | $19/2_2^- \rightarrow 15/2_1^-$ | | | 2171 | 0.02 |
| $^{135}$Xe | 2058 | 9.0(9) | 0.52(6) | $19/2_1^- \rightarrow 15/2_1^-$ | 2231 | 0.49 | 1972 | 0.02 |
| | | | | $19/2_2^- \rightarrow 15/2_1^-$ | 2449 | 2.29 | 2171 | 1.94 |
| $^{137}$Ba | 2349.9 | 589(20) | 0.46(3) | $19/2_1^- \rightarrow 15/2_1^-$ | 2595 | 0.31 | 2105 | 0.01 |
| | | | | $19/2_2^- \rightarrow 15/2_1^-$ | 2688 | 0.41 | 2452 | 1.19 |

is most probably of spin $23/2^-$. The $25/2^-$ state is only predicted above 3.5 MeV. Lower-spin states would preferably decay into states of spin $J < 19/2$. Consequently, the states at 3322, 3534.8, and 4232.7 keV are interpreted to have a spin of $J > 21/2$. Otherwise, they would directly decay to the $19/2^-$ state. The 3544.9-keV state is proposed to be the bandhead of a positive-parity band, which fits the systematics of the calculated level scheme. In the same way, the state at 4151.8 keV may be interpreted as either the $25/2^-$ or the $27/2^-$ state. However, due to the large density of predicted levels above 3.5 MeV, spins and parities cannot be assigned unambiguously solely on the basis of shell-model calculations.

Reduced transition probabilities [$B(E2)$ values] are calculated for the $(19/2^-) \rightarrow (15/2^-)$ transitions in $^{133}$Te, $^{135}$Xe, and $^{137}$Ba. The decays of both the first and the second excited states are considered. In the SN100PN calculations the effective neutron and proton charges are defined as $e_\nu = \delta e_\nu$ and $e_\pi = 1e + \delta e_\pi$ with polarization charges $\delta e_\nu = 0.81e$ and $\delta e_\pi = 0.52e$. The effective neutron polarization charge is tuned to reproduce the reduced transition strength of the first excited $2^+$ state in the $Z = 50$ isotope $^{128}$Sn, $B(E2; 2^+ \rightarrow 0^+) = 4.2(3)$ W.u. [70]. The obtained value of $\delta e_\nu = 0.81e$ is in very good agreement with the effective charges used in a previous study of the nearby nucleus $^{136}$Ba ($\delta e_{\pi,\nu} = 0.82e$) [59]. Keeping $\delta e_\nu$ fixed, $\delta e_\pi$ is modified to reproduce the $B(E2; 19/2^- \rightarrow 15/2^-)$ value in $^{133}$Te. In the PQM130 interaction, effective charges are chosen as $e_\nu = -0.60e - 0.10N_\nu\, e$ for neutrons and $e_\pi = +1.80e - 0.05N_\pi\, e$ for protons. $N_\pi$ and $N_\nu$ are the proton-particle and neutron-hole numbers with respect to $^{132}$Sn. Note that the neutron effective charge is chosen to be negative, as the calculations are performed for valence-neutron holes. The results are summarized in Table III. The $B(E2)$ value corresponding to the isomeric $(19/2^-) \rightarrow (15/2^-)$ transition in $^{133}$Te is well reproduced within the experimental error by the PQM130 interaction and by the SN100PN interaction with modified effective charges. However, the excitation energy of the isomeric state is overpredicted by the PQM130 interaction. In $^{135}$Xe the transition probability of the 310-keV transition deexciting the 9.0(9)-ns isomer at 2058 keV yields $B(E2) =$ 0.52(6) W.u. assuming a pure $E2$ multipolarity. The transition probability for the 120-keV transition deexciting the 589(20)-ns isomer at 2349.9 keV in $^{137}$Ba is 0.46(3) W.u. Particularly, the $B(E2)$ value of $^{135}$Xe is well reproduced by the PQM130 interaction. The calculation locates the second $19/2^-$ states slightly higher (0.2 MeV for $^{135}$Xe and 0.09 MeV for $^{137}$Ba) than the first $19/2^-$ states. Therefore, in $^{137}$Ba the calculated states might be reversed, i.e., the second calculated $19/2^-$ state might correspond to the first experimental $19/2^-$ state. In fact, the theoretical $B(E2)$ value of the second excited $19/2^-$ state obtained by the PQM130 interaction generally agrees with the experimental value of $^{137}$Ba. The SN100PN interaction does not reproduce the experimental $B(E2; 19/2^- \rightarrow 15/2^-)$ values for $^{135}$Xe and $^{137}$Ba. The Weisskopf hindrance factors of the $(19/2^-)$ isomers are $F_W = T_{1/2}^{\rm exp}/T_{1/2}^{\rm W} = 1.8$ for $^{135}$Xe and 1.1 for $^{137}$Ba, respectively.

The decomposition of the total angular momentum of the $15/2_1^-$, $19/2_1^-$, and $19/2_2^-$ states in $^{133}$Te, $^{135}$Xe, and $^{137}$Ba into their neutron ($I_\nu$) and proton ($I_\pi$) spin components in the SN100PN calculation is presented in Fig. 11 while Table IV shows the average proton occupation numbers of each orbital of the *gdsh* model space for the $15/2_1^-$, $19/2_1^-$, and $19/2_2^-$ states in the PQM130 and SN100PN calculations. The decay of the $19/2^-$ isomer to the $15/2^-$ state in $^{133}$Te is comparable to the isomeric $\pi g_{7/2}^2 \rightarrow \pi g_{7/2}^2$ $6^+ \rightarrow 4^+$ transition in the neighboring $N = 82$ nucleus $^{134}$Te, and the $B(E2; 19/2^- \rightarrow 15/2^-)$ in $^{133}$Te is found to be only slightly larger than the $B(E2; 6^+ \rightarrow 4^+)$ in $^{134}$Te [71]. The SN100PN interaction computes the first excited $19/2^-$ and $15/2^-$ states to have $\nu h_{11/2}^{-1} \otimes \pi g_{7/2}^2$ configurations with fractions of 88% and 92%, respectively. The $15/2_1^-$ state is predicted to have a 75% fully stretched [$\nu\, 11/2^- \otimes \pi\, 2^+$] and a 21% [$\nu\, 11/2^- \otimes \pi\, 4^+$] configuration, whereas the $19/2_1^-$ state is predominantly $\nu\, 11/2^-$ coupled to $\pi$-$4^+$ (41%) and $\pi$-$6^+$ (58%) configurations. The similar $g_{7/2}$ occupation numbers of the $19/2^-$ and $15/2^-$ states in both interactions (see Table IV) emphasize the $\pi g_{7/2}^2 \rightarrow \pi g_{7/2}^2$ character of the $19/2_1^- \rightarrow 15/2_1^-$ transition which $B(E2)$ is well reproduced by both calculations (see Table III). For the $19/2_2^-$ state, the occupancy of the $d_{5/2}$ orbital is predicted to be much larger by the SN100PN calculation.

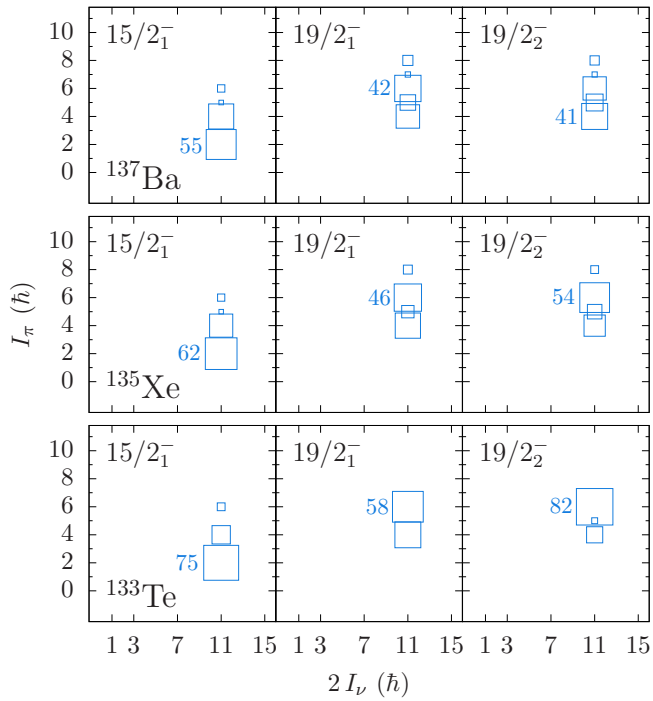


FIG. 11. Decomposition of the total angular momentum of the $15/2_1^-$, $19/2_1^-$, and $19/2_2^-$ states in $^{133}$Te, $^{135}$Xe, and $^{137}$Ba into their neutron ($I_\nu$) and proton ($I_\pi$) spin components in the SN100PN calculation. The area of the boxes corresponds to the percentage of the particular $I_\nu \otimes I_\pi$ configuration. Percentages above 1% are shown; percentages of the largest component are also given in numbers for scale.

TABLE IV. Average proton occupation numbers in each single-particle orbit of the *gdsh* model space for the $15/2_1^-$, $19/2_1^-$, and $19/2_2^-$ states in $^{133}$Te, $^{135}$Xe, and $^{137}$Ba, calculated using the SN100PN and the PQM130 interactions.

| Isotope | $J^\pi$ | $g_{7/2}$ | $d_{5/2}$ | $d_{3/2}$ | $s_{1/2}$ | $h_{11/2}$ |
|---|---|---|---|---|---|---|
| | | PQM130 | | | | |
| $^{133}$Te | $15/2_1^-$ | 1.96 | 0.01 | 0.02 | 0.00 | 0.00 |
| | $19/2_1^-$ | 1.97 | 0.02 | 0.01 | 0.00 | 0.00 |
| | $19/2_2^-$ | 1.96 | 0.02 | 0.02 | 0.00 | 0.00 |
| $^{135}$Xe | $15/2_1^-$ | 3.28 | 0.51 | 0.12 | 0.03 | 0.06 |
| | $19/2_1^-$ | 3.45 | 0.39 | 0.08 | 0.02 | 0.06 |
| | $19/2_2^-$ | 3.28 | 0.55 | 0.08 | 0.03 | 0.06 |
| $^{137}$Ba | $15/2_1^-$ | 4.06 | 1.46 | 0.23 | 0.12 | 0.13 |
| | $19/2_1^-$ | 4.36 | 1.30 | 0.15 | 0.06 | 0.13 |
| | $19/2_2^-$ | 4.37 | 1.28 | 0.15 | 0.07 | 0.13 |
| | | SN100PN | | | | |
| $^{133}$Te | $15/2_1^-$ | 1.90 | 0.06 | 0.02 | 0.01 | 0.01 |
| | $19/2_1^-$ | 1.88 | 0.11 | 0.01 | 0.00 | 0.00 |
| | $19/2_2^-$ | 1.09 | 0.89 | 0.01 | 0.01 | 0.00 |
| $^{135}$Xe | $15/2_1^-$ | 3.00 | 0.69 | 0.12 | 0.05 | 0.14 |
| | $19/2_1^-$ | 3.05 | 0.71 | 0.09 | 0.03 | 0.12 |
| | $19/2_2^-$ | 2.97 | 0.84 | 0.07 | 0.03 | 0.09 |
| $^{137}$Ba | $15/2_1^-$ | 3.48 | 1.81 | 0.25 | 0.13 | 0.34 |
| | $19/2_1^-$ | 3.75 | 1.70 | 0.18 | 0.08 | 0.28 |
| | $19/2_2^-$ | 3.74 | 1.67 | 0.19 | 0.10 | 0.30 |

Likewise, the observed high-spin level structures in $^{135}$Xe and $^{137}$Ba are interpreted as the coupling of the $h_{11/2}$ neutron hole to proton configurations. However, the theoretical wave functions of the high-spin states are much more complex and fragmented than in $^{133}$Te. While the character of the $19/2^- \rightarrow 15/2^-$ transition is clear for $^{133}$Te, it is not trivial for $^{135}$Xe and $^{137}$Ba. In $^{135}$Xe, the first two $19/2^-$ states are predicted by the PQM130 interaction to consist mainly (64%) of the $(\nu h_{11/2}^{-1} \otimes \pi g_{7/2}^4)$ configuration, approximately 23% of the $(\nu h_{11/2}^{-1} \otimes \pi g_{7/2}^3 d_{5/2}^1)$ configuration, and about 9% of the $(\nu h_{11/2}^{-1} \otimes \pi g_{7/2}^2 d_{5/2}^2)$ configuration. The SN100PN interaction computes the $19/2_1^-$ state as a mixture of 42% $(\nu h_{11/2}^{-1} \otimes \pi g_{7/2}^4)$ and 26% $(\nu h_{11/2}^{-1} \otimes \pi g_{7/2}^3 d_{5/2}^1)$ configurations. The $19/2_2^-$ state is predicted to have a dominant 51% $\nu h_{11/2}^{-1} \otimes \pi g_{7/2}^3 d_{5/2}^1$ and a 26% $\nu h_{11/2}^{-1} \otimes \pi g_{7/2}^4$ configuration. Couplings of the $\nu h_{11/2}^{-1}$ hole to proton configurations with spins of $4^+$ (28%), $5^+$ (13%), and $6^+$ (54%) contribute to the configuration of the $19/2_2^-$ state. The calculated $B(E2; 19/2_2^- \rightarrow 15/2_1^-)$ value reproduces the experimental transition strength better than the decay of the corresponding $19/2_1^-$ state, although overestimating it. The SN100PN interaction predicts in $^{135}$Xe a higher degree of $d_{5/2}$ occupancy than in $^{133}$Te (see Table IV). A similar situation is found in $^{137}$Ba, suggesting a reduced spacing between the $\pi g_{7/2}$ and $\pi d_{5/2}$ orbitals. Both the SN100PN and PQM130 interactions predict the $19/2_{1,2}^-$ states in $^{137}$Ba to mainly consist of the $[\nu h_{11/2}^{-1} \otimes \pi (g_{7/2} d_{5/2})^6]$ configuration. The configurations are predicted to be highly fragmented. Like in $^{135}$Xe, the occupation numbers are almost the same between the two $19/2^-$ states, but internal couplings are different. The $g_{7/2}^6$ configuration is nearly missing in the SN100PN calculation, which is further evidence for easy redistribution of protons from $g_{7/2}$ to $d_{5/2}$ orbitals, i.e., these orbitals are close together. Continuing the analogy to the isomeric $6^+ \rightarrow 4^+$ decays along the $N = 82$ isotones, the SN100PN interaction yields the transition probability of the $19/2_1^- \rightarrow 15/2_1^-$ decay to be 0.02 W.u. in $^{135}$Xe and 0.01 W.u. in $^{137}$Ba, missing the experimental transition strengths (see Table III) by an order of magnitude; but they are very similar to the measured values of $B(E2; 6^+ \rightarrow 4^+) = 0.013(1)$ W.u. in $^{136}$Xe [72] and 0.055(7) W.u. in $^{138}$Ba [73]. Therefore, we assume that the calculated proton configurations follow the nuclear structure of the closed $N = 82$ shell nuclei, validating the proton-proton part of the SN100PN interaction. Thus, most probably, the proton-neutron part falls short in reproducing the decay features of the isomeric states in $^{135}$Xe and $^{137}$Ba. Similar conclusions were discussed in Ref. [74]. There, the *p-n* monopole part of the SN100PN interaction was replaced by new shell-model developments. The new interaction combines the well-established proton-proton part of the SN100PN interaction with the semiempirical SNBG3 neutron-neutron interaction by Honma *et al.* [75] and the novel universal $V_{\rm MU}$ interaction [76] for the proton-neutron part. The SNBG3 interaction is obtained by combining the next-to-next-to-next-to-leading order ($N^3$LO) interaction with a $\chi^2$ fit of levels including $3^-$ states in $50 < N < 82$ Sn isotopes. The interaction successfully described the shell evolution along Sb isotopes

[74] and may provide insight into Xe and Ba isotopes in the future.

## V. CONCLUSIONS

In summary, four experiments employing the $^{136}$Xe + $^{198}$Pt, $^{136}$Xe + $^{208}$Pb, and $^{136}$Xe + $^{238}$U multinucleon-transfer reactions as well as the $^{11}$B + $^{130}$Te fusion-evaporation reaction were used to measure lifetimes of high-spin isomers and to establish high-spin states in $^{135}$Xe and $^{137}$Ba. Several new levels and $\gamma$-ray transitions are assigned to $^{135}$Xe. The level scheme of $^{137}$Ba is extended up to an excitation energy of 5.0 MeV. The half-life of the 2058-keV $(19/2^-)$ state in $^{135}$Xe is measured to be 9.0(9) ns, corresponding to a transition probability of $B(E2,19/2^- \rightarrow 15/2^-) = 0.52(6)$ W.u. The identification of this isomeric state completes the systematics for the $N = 81$ isotones. Large-scale shell-model calculations employing the novel PQM130 interaction perform well in predicting electromagnetic transition probabilities of high-spin isomers in the $N = 81$ isotones that cannot be reproduced by the SN100PN interaction. Some ambiguities remain for the interpretation of high-spin states in both interactions. In the future, a novel microscopic effective interaction by Utsuno, Otsuka, Shimizu *et al.* [74] may provide a more unified description of the $50 \leqslant Z,N \leqslant 82$ shells.

Although $^{137}$Ba and $^{135}$Xe are stable or located between two stable isotopes, respectively, there is a lack of beam and target combinations to populate high spins via nuclear reactions. Refined detection capabilities are needed to address these indeed hard-to-reach nuclei via MNT or fission reactions. In future, detailed angular correlation and polarization measurements are desirable to determine proper spin, parity, and multipolarity assignments. In perspective, the extended AGATA spectrometer coupled to the Variable Mode Spectrometer at the Grand Accélérateur National d'Ions Lourds will allow for a more detailed spectroscopy of the $N = 81$ nuclei.

## ACKNOWLEDGMENTS

We thank the IKP FN Tandem accelerator team for the professional support during the experiment. The research leading to these results has received funding from the German BMBF under Contract No. 05P12PKFNE TP4, from the European Union Seventh Framework Programme FP7/2007-2013 under Grant Agreement No. 262010-ENSAR, from the Spanish Ministerio de Ciencia e Innovación under Contract No. FPA2011-29854-C04, from the Spanish Ministerio de Economía y Competitividad under Contract No. FPA2014-57196-C5, from the UK Science and Technology Facilities Council (STFC), and from the US National Science Foundation (NSF). E.T. and N.Y. were supported by a Grant-in-Aid for Japan Society for the Promotion of Science (JSPS) Fellows (Grant No. 26.10429). A.V. and L.K. thank the Bonn-Cologne Graduate School of Physics and Astronomy (BCGS) for financial support. One of the authors (A. Gadea) has been supported by the Generalitat Valenciana, Spain, under the grant PROMETEOII/2014/019, and by the EU under the Fonds Européen de Développement Économique et Régional program.

[1] B. A. Brown, N. J. Stone, J. R. Stone, I. S. Towner, and M. Hjorth-Jensen, Magnetic moments of the $2_1^+$ states around $^{132}$Sn, Phys. Rev. C **71**, 044317 (2005).

[2] K. Higashiyama and N. Yoshinaga, Pair-truncated shell-model analysis of nuclei around mass 130, Phys. Rev. C **83**, 034321 (2011).

[3] E. Teruya, N. Yoshinaga, K. Higashiyama, and A. Odahara, Shell-model calculations of nuclei around mass 130, Phys. Rev. C **92**, 034320 (2015).

[4] L. Coraggio, A. Covello, A. Gargano, N. Itaco, and T. T. S. Kuo, Shell-model study of the $N = 82$ isotonic chain with a realistic effective Hamiltonian, Phys. Rev. C **80**, 044320 (2009).

[5] E. Caurier, F. Nowacki, A. Poves, and K. Sieja, Collectivity in the light xenon isotopes: A shell model study, Phys. Rev. C **82**, 064304 (2010).

[6] A. Astier, M.-G. Porquet, Ch. Theisen, D. Verney, I. Deloncle, M. Houry, R. Lucas, F. Azaiez, G. Barreau, D. Curien, O. Dorvaux, G. Duchêne, B. J. P. Gall, N. Redon, M. Rousseau, and O. Stézowski, High-spin states with seniority $v = 4$, 5, and 6 in $^{119-126}$Sn, Phys. Rev. C **85**, 054316 (2012).

[7] Ł. W. Iskra, R. Broda, R. V. F. Janssens, C. J. Chiara, M. P. Carpenter, B. Fornal, N. Hoteling, F. G. Kondev, W. Królas, T. Lauritsen, T. Pawłat, D. Seweryniak, I. Stefanescu, W. B. Walters, J. Wrzesiński, and S. Zhu, Shell-model states with seniority $v = 3$, 5, and 7 in odd-$A$ neutron-rich Sn isotopes, Phys. Rev. C **93**, 014303 (2016).

[8] A. Astier, M.-G. Porquet, Ts. Venkova, D. Verney, Ch. Theisen, G. Duchêne, F. Azaiez, G. Barreau, D. Curien, I. Deloncle, O. Dorvaux, B. J. P. Gall, M. Houry, R. Lucas, N. Redon, M. Rousseau, and O. Stézowski, High-spin structures of five $N = 82$ isotopes: $^{136}_{54}$Xe, $^{137}_{55}$Cs, $^{138}_{56}$Ba, $^{139}_{57}$La, and $^{140}_{58}$Ce, Phys. Rev. C **85**, 064316 (2012).

[9] P. C. Srivastava, M. J. Ermamatov, and Irving O. Morales, High-spin structures of $^{136}_{54}$Xe, $^{137}_{55}$Cs, $^{138}_{56}$Ba, $^{139}_{57}$La, and $^{140}_{58}$Ce: a shell model description, J. Phys. G **40**, 035106 (2013).

[10] A. Astier, M. G. Porquet, Ts. Venkova, Ch. Theisen, G. Duchêne, F. Azaiez, G. Barreau, D. Curien, I. Deloncle, O. Dorvaux, B. J. P. Gall, M. Houry, R. Lucas, N. Redon, M. Rousseau, and O. Stézowski, High-spin structures of $^{124-131}$Te: Competition of proton- and neutron-pair breakings, Eur. Phys. J. A **50**, 1 (2014).

[11] V. Kumar, P. C. Srivastava, M. J. Ermamatov, and I. O. Morales, Analysis of proton and neutron pair breakings: High-spin structures of $^{124-127}$Te isotopes, Nucl. Phys. A **942**, 1 (2015).

[12] S. Biswas, R. Palit, A. Navin, M. Rejmund, A. Bisoi, M. S. Sarkar, S. Sarkar, S. Bhattacharyya, D. C. Biswas, M. Caamaño, M. P. Carpenter, D. Choudhury, E. Clément, L. S. Danu, O. Delaune, F. Farget, G. de France, S. S. Hota, B. Jacquot, A. Lemasson, S. Mukhopadhyay, V. Nanal, R. G. Pillay, S. Saha, J. Sethi, Purnima Singh, P. C. Srivastava, and S. K. Tandel, Structure of $^{132}_{52}$Te$_{80}$: The two-particle and two-hole spectrum of $^{132}_{50}$Sn$_{82}$, Phys. Rev. C **93**, 034324 (2016).

[13] W. B. Walters, S. M. Lane, N. L. Smith, R. J. Nagle, and R. A. Meyer, Shell model description of $N = 81$ five-exciton $^{135}$Xe and the decay of $^{135}$I, Phys. Rev. C **26**, 2273 (1982).

[14] J. A. C. Gonçalves and R. N. Saxena, Directional correlations of $\gamma$ transitions in $^{135}$Xe following the decay of $^{135}$I, Phys. Rev. C **43**, 2586 (1991).

[15] B. Singh, A. A. Rodionov, and Y. L. Khazov, Nuclear data sheets for $A = 135$, Nucl. Data Sheets **109**, 517 (2008).

[16] H. Götte, Eine bei der Uranspaltung auftretende Kernisomerie bei Xenon, Naturwissenschaften **28**, 449 (1940).

[17] C.-S. Wu and E. Segrè, Radioactive Xenons, Phys. Rev. **67**, 142 (1945).

[18] N. Fotiades, R. O. Nelson, M. Devlin, J. A. Cizewski, J. A. Becker, W. Younes, R. Krücken, R. M. Clark, P. Fallon, I. Y. Lee, A. O. Macchiavelli, T. Ethvignot, and T. Granier, High-spin states in $^{135}$Xe, Phys. Rev. C **75**, 054322 (2007).

[19] B. K. Wagner, P. E. Garrett, M. Yeh, and S. W. Yates, On the first excited state of $^{137}$Ba, J. Radioanal. Nucl. Chem. **219**, 217 (1997).

[20] I. Bikit, I. Aničin, J. Slivka, M. Krmar, J. Puzović, and Lj. Čonkić, Population of the 283 keV level of $^{137}$Ba by the $\beta$ decay of $^{137}$Cs, Phys. Rev. C **54**, 3270 (1996).

[21] V. A. Bondarenko, I. L. Kuvaga, P. T. Prokofjev, A. M. Sukhovoj, V. A. Khitrov, Yu. P. Popov, S. Brant, and V. Paar, Levels of $^{137}$Ba studied with neutron-induced reactions, Nucl. Phys. A **582**, 1 (1995).

[22] E. Dragulescu, M. Ivascu, R. Mihu, D. Popescu, G. Semenescu, A. Velenik, and V. Paar, Coulomb excitation of levels in $^{135}$Ba and $^{137}$Ba, J. Phys. G **10**, 1099 (1984).

[23] E. Browne and J. K. Tuli, Nuclear data sheets for $A = 137$, Nucl. Data Sheets **108**, 2173 (2007).

[24] K. Moran, E. A. McCutchan, C. J. Lister, S. Zhu, M. P. Carpenter, P. Chowdhury, J. P. Greene, T. Lauritsen, E. Merchan, and R. Shearman, $E5$ decay from the $J^\pi = 11/2^-$ isomer in $^{137}$Ba, Phys. Rev. C **90**, 041303 (2014).

[25] C. Walz, H. Scheit, N. Pietralla, T. Aumann, R. Lefol, and V. Yu Ponomarev, Observation of the competitive double-gamma nuclear decay, Nature (London) **526**, 406 (2015).

[26] A. Kerek and J. Kownacki, The level structure of the $N = 81$ and 82 nucleides $^{137,138}$Ba as investigated in $^{136}$Xe$(\alpha,xn)$ reactions, Nucl. Phys. A **206**, 245 (1973).

[27] Evaluated Nuclear Structure Data File (ENSDF), online resource: http://www.nndc.bnl.gov/ensdf/

[28] P. Bhattacharyya, P. J. Daly, C. T. Zhang, Z. W. Grabowski, S. K. Saha, R. Broda, B. Fornal, I. Ahmad, D. Seweryniak, I. Wiedenhöver, M. P. Carpenter, R. V. F. Janssens, T. L. Khoo, T. Lauritsen, C. J. Lister, P. Reiter, and J. Blomqvist, Magic Nucleus $^{132}$Sn and Its One-Neutron-Hole Neighbor $^{131}$Sn, Phys. Rev. Lett. **87**, 062502 (2001).

[29] B. Fogelberg, H. Gausemel, K. A. Mezilev, P. Hoff, H. Mach, M. Sanchez-Vega, A. Lindroth, E. Ramström, J. Genevey, J. A. Pinston, and M. Rejmund, Decays of $^{131}$In, $^{131}$Sn, and the position of the $h_{11/2}$ neutron hole state, Phys. Rev. C **70**, 034312 (2004).

[30] J. K. Hwang, A. V. Ramayya, J. H. Hamilton, C. J. Beyer, J. O. Rasmussen, Y. X. Luo, S. C. Wu, T. N. Ginter, C. M. Folden, P. Fallon, P. M. Zielinski, K. E. Gregorich, A. O. Macchiavelli, M. Stoyer, S. J. Asztalos, A. Covello, and A. Gargano, Particle-hole excited states in $^{133}$Te, Phys. Rev. C **65**, 034319 (2002).

[31] S. Kaim, C. M. Petrache, A. Gargano, N. Itaco, T. Zerrouki, R. Leguillon, A. Astier, I. Deloncle, T. Konstantinopoulos, J. M. Régis, D. Wilmsen, B. Melon, A. Nannini, C. Ducoin, D. Guinet, and T. Bhattacharjee, High-spin spectroscopy of $^{139}$Ce, Phys. Rev. C **91**, 024318 (2015).

[32] T. Zerrouki, C. M. Petrache, R. Leguillon, K. Hauschild, A. Korichi, A. Lopez-Martens, S. Frauendorf, I. Ragnarsson, H. Hübel, A. Neußer-Neffgen, A. Al-Khatib, P. Bringel, A. Bürger, N. Nenoff, G. Schönwaßer, A. K. Singh, D. Curien, G. B. Hagemann, B. Herskind, G. Sletten, P. Fallon, A. Görgen, and P. Bednarczyk, Shape evolution and magnetic rotation in $^{141}$Nd, Eur. Phys. J. A **51**, 1 (2015).

[33] J. Ludziejewski, J. Bialkowski, Z. Haratym, L.-E. de Geer, A. Kerek, and J. Kozyczkowski, The life-time measurements of some high-spin states in the $^{138,139}$Ce and $^{141,142}$Nd nuclei, Phys. Scr. **14**, 133 (1976).

[34] A. Pakkanen, J. Muhonen, M. Piiparinen, and J. Blomqvist, Medium-spin levels and the character of the 20.4 ns $13/2^+$ isomer in $^{145}$Gd, Nucl. Phys. A **373**, 237 (1982).

[35] K. Heyde and P. J. Brussaard, Neutron hole states in the $N = 81$ nuclei, Z. Phys. A **259**, 15 (1972).

[36] K. Kotajima and H. Morinaga, Isomers in $N = 81$ Nuclei, Nucl. Phys. **16**, 231 (1960).

[37] Yu. Khazov, A. Rodionov, and F. G. Kondev, Nuclear data sheets for $A = 133$, Nucl. Data Sheets **112**, 855 (2011).

[38] S. Chanda, T. Bhattacharjee, S. Bhattacharyya, A. Mukherjee, S. Kumar Basu, I. Ragnarsson, R. K. Bhowmik, S. Muralithar, R. P. Singh, S. S. Ghugre, and U. D. Pramanik, Seven-quasiparticle bands in $^{139}$Ce, Phys. Rev. C **79**, 054332 (2009).

[39] T. W. Burrows, Nuclear data sheets for $A = 139$, Nucl. Data Sheets **92**, 623 (2001).

[40] D. A. Volkov, B. A. Gorbachev, A. I. Levon, O. F. Nemets, and V. A. Stepanenko, Measurement of the nuclear $g$ factor of the $19/2^-$ isomer in $^{139}$Ce, Yad. Fiz. **40**, 289 (1984) [Sov. J. Nucl. Phys. **40**, 183 (1984)].

[41] S. Bhowal, C. Lahiri, R. Raut, P. Singh, M. Kumar Raju, A. Goswami, A. K. Singh, S. Bhattacharya, T. Bhattacharjee, G. Mukherjee, S. Bhattacharyya, S. Muralithar, R. K. Bhowmik, N Madhavan, R. P. Singh, and G. Gangopadhyay, Energy levels in $^{141}$Nd from fusion evaporation study, J. Phys. G **38**, 035105 (2011).

[42] J. Kownacki, J. Ludziejewski, Z. Sujkowski, H. Arnold, and H. Ryde, High-spin states and evidence for hole-core coupling in the $^{143}$Sm$_{81}$ and $^{145}$Gd$_{81}$ nuclei, Nucl. Phys. A **236**, 125 (1974).

[43] R. Raut, S. Ganguly, R. Kshetri, P. Banerjee, S. Bhattacharya, B. Dasmahapatra, A. Mukherjee, G. Mukherjee, M. Saha Sarkar, A. Goswami, G. Gangopadhyay, S. Mukhopadhyay, Krishichayan, A. Chakraborty, S. S. Ghughre, T. Bhattacharjee, and S. K. Basu, High spin states in $^{143}$Sm, Phys. Rev. C **73**, 044305 (2006).

[44] S. Akkoyun *et al.*, AGATA–Advanced GAmma Tracking Array, Nucl. Instrum. Methods Phys. Res., Sect. A **668**, 26 (2012).

[45] A. M. Stefanini, L. Corradi, G. Maron, A. Pisent, M. Trotta, A. M. Vinodkumar, S. Beghini, G. Montagnoli, F. Scarlassara, G. F. Segato, A. De Rosa, G. Inglima, D. Pierroutsakou, M. Romoli, M. Sandoli, G. Pollarolo, and A. Latina, The heavy-ion magnetic spectrometer PRISMA, Nucl. Phys. A **701**, 217 (2002).

[46] S. Szilner, C. A. Ur, L. Corradi, N. Marginean, G. Pollarolo, A. M. Stefanini, S. Beghini, B. R. Behera, E. Fioretto, A. Gadea, B. Guiot, A. Latina, P. Mason, G. Montagnoli, F. Scarlassara, M. Trotta, G. de Angelis, F. Della Vedova, E. Farnea, F. Haas, S. Lenzi, S. Lunardi, R. Marginean, R. Menegazzo, D. R. Napoli, M. Nespolo, I. V. Pokrovsky, F. Recchia, M. Romoli, M.-D.

Salsac, N. Soić, and J. J. Valiente-Dobón, Multinucleon transfer reactions in closed-shell nuclei, Phys. Rev. C **76**, 024604 (2007).

[47] L. Corradi, S. Szilner, G. Pollarolo, D. Montanari, E. Fioretto, A. M. Stefanini, J. J. Valiente-Dobón, E. Farnea, C. Michelagnoli, G. Montagnoli, F. Scarlassara, C. A. Ur, T. Mijatović, D. Jelavić Malenica, N. Soić, and F. Haas, Multinucleon transfer reactions: Present status and perspectives, Nucl. Instrum. Methods Phys. Res., Sect. B **317, Part B**, 743 (2013).

[48] I-Yang Lee, The GAMMASPHERE, Nucl. Phys. A **520**, c641 (1990).

[49] M. W. Simon, D. Cline, C. Y. Wu, R. W. Gray, R. Teng, and C. Long, CHICO, a heavy ion detector for Gammasphere, Nucl. Instrum. Methods Phys. Res., Sect. A **452**, 205 (2000).

[50] L. Netterdon, V. Derya, J. Endres, C. Fransen, A. Hennig, J. Mayer, C. Müller-Gatermann, A. Sauerwein, P. Scholz, M. Spieker, and A. Zilges, The $\gamma$-ray spectrometer HORUS and its applications for nuclear astrophysics, Nucl. Instrum. Methods Phys. Res., Sect. A **754**, 94 (2014).

[51] A. Gadea, E. Farnea, J. J. Valiente-Dobón, B. Million, D. Mengoni, D. Bazzacco, F. Recchia, A. Dewald, Th. Pissulla, W. Rother, G. de Angelis *et al.*, Conceptual design and infrastructure for the installation of the first AGATA sub-array at LNL, Nucl. Instrum. Methods Phys. Res., Sect. A **654**, 88 (2011).

[52] A. Wiens, H. Hess, B. Birkenbach, B. Bruyneel, J. Eberth, D. Lersch, G. Pascovici, P. Reiter, and H.-G. Thomas, The AGATA triple cluster detector, Nucl. Instrum. Methods Phys. Res., Sect. A **618**, 223 (2010).

[53] B. Bruyneel, B. Birkenbach, and P. Reiter, Pulse shape analysis and position determination in segmented HPGe detectors: The AGATA detector library, Eur. Phys. J. A **52**, 70 (2016).

[54] A. Lopez-Martens, K. Hauschild, A. Korichi, J. Roccaz, and J.-P. Thibaud, $\gamma$-ray tracking algorithms: A comparison, Nucl. Instrum. Methods Phys. Res., Sect. A **533**, 454 (2004).

[55] A. Vogt, B. Birkenbach, P. Reiter, L. Corradi, T. Mijatović, D. Montanari, S. Szilner, D. Bazzacco, M. Bowry, A. Bracco, B. Bruyneel, F. C. L. Crespi, G. de Angelis, P. Désesquelles, J. Eberth, E. Farnea, E. Fioretto, A. Gadea, K. Geibel, A. Gengelbach, A. Giaz, A. Görgen, A. Gottardo, J. Grebosz, H. Hess, P. R. John, J. Jolie, D. S. Judson, A. Jungclaus, W. Korten, S. Leoni, S. Lunardi, R. Menegazzo, D. Mengoni, C. Michelagnoli, G. Montagnoli, D. Napoli, L. Pellegri, G. Pollarolo, A. Pullia, B. Quintana, F. Radeck, F. Recchia, D. Rosso, E. Şahin, M. D. Salsac, F. Scarlassara, P.-A. Söderström, A. M. Stefanini, T. Steinbach, O. Stezowski, B. Szpak, Ch. Theisen, C. Ur, J. J. Valiente-Dobón, V. Vandone, and A. Wiens, Light and heavy transfer products in $^{136}$Xe $+^{238}$U multinucleon transfer reactions, Phys. Rev. C **92**, 024619 (2015).

[56] A. B. Brown, C. W. Snyder, W. A. Fowler, and C. C. Lauritsen, Excited States of the Mirror Nuclei, $^{7}$Li and $^{7}$Be, Phys. Rev. **82**, 159 (1951).

[57] R. S. Kempley *et al.*, Cross Coincidences in the $^{136}$Xe $+^{208}$Pb deep-inelastic reaction, Acta. Phys. Pol. B **42**, 717 (2011).

[58] M. Siciliano *et al.*, Neutron-rich nuclei in the vicinity of $^{208}$Pb, LNL Annual Report 2014 **241**, 63 (2015).

[59] J. J. Valiente-Dobón, P. H. Regan, C. Wheldon, C. Y. Wu, N. Yoshinaga, K. Higashiyama, J. F. Smith, D. Cline, R. S. Chakrawarthy, R. Chapman, M. Cromaz, P. Fallon, S. J. Freeman, A. Görgen, W. Gelletly, A. Hayes, H. Hua, S. D. Langdown, I. Y. Lee, X. Liang, A. O. Macchiavelli, C. J. Pearson, Zs. Podolyák, G. Sletten, R. Teng, D. Ward, D. D. Warner, and A. D. Yamamoto, $^{136}$Ba studied via deep-inelastic collisions: Identification of the $(\nu h_{11/2})^{-2}_{10+}$ isomer, Phys. Rev. C **69**, 024316 (2004).

[60] D. C. Radford, ESCL8R and LEVIT8R: Software for interactive graphical analysis of HPGe coincidence data sets, Nucl. Instrum. Methods Phys. Res., Sect. A **361**, 297 (1995).

[61] O. B. Tarasov and D. Bazin, Development of the program LISE: Application to fusion-evaporation, in *14th International Conference on Electromagnetic Isotope Separators and Techniques Related to their Applications* [Nucl. Instrum. Methods Phys. Res., Sect. B **204**, 174 (2003)].

[62] F. Pühlhofer, On the interpretation of evaporation residue mass distributions in heavy-ion induced fusion reactions, Nucl. Phys. A **280**, 267 (1977).

[63] N. Saed-Samii, Diplomarbeit, Universität zu Köln, 2013 (unpublished).

[64] J. Theuerkauf, Ph.D. thesis, Universität zu Köln, 1994.

[65] A. Vogt, B. Birkenbach, P. Reiter, A. Blazhev, M. Siciliano, J. J. Valiente-Dobón, C. Wheldon, D. Bazzacco, M. Bowry, A. Bracco, B. Bruyneel, R. S. Chakrawarthy, R. Chapman, D. Cline, L. Corradi, F. C. L. Crespi, M. Cromaz, G. de Angelis, J. Eberth, P. Fallon, E. Farnea, E. Fioretto, S. J. Freeman, A. Gadea, K. Geibel, W. Gelletly, A. Gengelbach, A. Giaz, A. Görgen, A. Gottardo, A. B. Hayes, H. Hess, H. Hua, P. R. John, J. Jolie, A. Jungclaus, W. Korten, I. Y. Lee, S. Leoni, X. Liang, S. Lunardi, A. O. Macchiavelli, R. Menegazzo, D. Mengoni, C. Michelagnoli, T. Mijatović, G. Montagnoli, D. Montanari, D. Napoli, C. J. Pearson, L. Pellegri, Zs. Podolyák, G. Pollarolo, A. Pullia, F. Radeck, F. Recchia, P. H. Regan, E. Şahin, F. Scarlassara, G. Sletten, J. F. Smith, P.-A. Söderström, A. M. Stefanini, T. Steinbach, O. Stezowski, S. Szilner, B. Szpak, R. Teng, C. Ur, V. Vandone, D. Ward, D. D. Warner, A. Wiens, and C. Y. Wu, High-spin structure of $^{134}$Xe, Phys. Rev. C **93**, 054325 (2016).

[66] A. A. Sonzogni, Nuclear data sheets for $A = 136$, Nucl. Data Sheets **95**, 837 (2002).

[67] B. A. Brown and W. D. M. Rae, The shell-model code NuShellX@MSU, Nucl. Data Sheets **120**, 115 (2014).

[68] R. Machleidt, F. Sammarruca, and Y. Song, Nonlocal nature of the nuclear force and its impact on nuclear structure, Phys. Rev. C **53**, R1483 (1996).

[69] T. Kibédi, T. W. Burrows, M. B. Trzhaskovskaya, P. M. Davidson, and C. W. Nestor, Jr., Evaluation of theoretical conversion coefficients using BrIcc, Nucl. Instrum. Methods Phys. Res., Sect. A **589**, 202 (2008).

[70] J. M. Allmond, D. C. Radford, C. Baktash, J. C. Batchelder, A. Galindo-Uribarri, C. J. Gross, P. A. Hausladen, K. Lagergren, Y. Larochelle, E. Padilla-Rodal, and C.-H. Yu, Coulomb excitation of $^{124,126,128}$Sn, Phys. Rev. C **84**, 061303 (2011).

[71] P. Bhattacharyya, P. J. Daly, C. T. Zhang, Z. W. Grabowski, S. K. Saha, B. Fornal, R. Broda, W. Urban, I. Ahmad, D. Seweryniak, I. Wiedenhöver, M. P. Carpenter, R. V. F. Janssens, T. L. Khoo, T. Lauritsen, C. J. Lister, P. Reiter, and J. Blomqvist, Yrast excitations in $N = 81$ nuclei $^{132}$Sb and $^{133}$Te from $^{248}$Cm fission, Phys. Rev. C **64**, 054312 (2001).

[72] A. A. Sonzogni, Nuclear data sheets for $A = 134$, Nucl. Data Sheets **103**, 1 (2004).
[73] A. A. Sonzogni, Nuclear data sheets for $A = 138$, Nucl. Data Sheets **98**, 515 (2003).
[74] Y. Utsuno, T. Otsuka, N. Shimizu, M. Honma, T. Mizusaki, Y. Tsunoda, and T. Abe, Recent shell-model results for exotic nuclei, EPJ Web Conf. **66**, 02106 (2014).
[75] M. Honma, T. Otsuka, T. Mizusaki, and M. Hjorth-Jensen, Shell-model fits for Sn isotopes, RIKEN Accel. Prog. Rep. **45**, 35 (2012).
[76] T. Otsuka, T. Suzuki, M. Honma, Y. Utsuno, N. Tsunoda, K. Tsukiyama, and M. Hjorth-Jensen, Novel Features of Nuclear Forces and Shell Evolution in Exotic Nuclei, Phys. Rev. Lett. **104**, 012501 (2010).